Supplementary Materials for

Positive feedback between PU.1 and the cell cycle controls myeloid differentiation

Hao Yuan Kueh, Ameya Champhekhar, Stephen L. Nutt, Michael B. Elowitz and Ellen V. Rothenberg

correspondence to: evroth@its.caltech.edu

This PDF file includes:

MATERIALS AND METHODS

Animals

PU.1-GFP mice were obtained from the Walter and Eliza Hall Institute, crossed to B6 mice to separate the PU.1-GFP locus from the tamoxifen-inducible Cre transgene present in the parental strain, and bred and maintained in the Caltech Laboratory Animal Facility. E13.5 fetuses were obtained by timed-mating of PU.1-GFP mice. All animal protocols were reviewed and approved by the Institute Animal Care and Use Committee of the California Institute of Technology.

Constructs and Reagents

An internal ribosome entry site (IRES)-mCherry fluorescent protein cassette and an IRES-Histone-2B-mCerulean CFP fluorescent protein cassette were generated using PCR cloning and inserted into an NGFR derivative of the pMIGR1 retroviral vector kindly provided by Lanwei Xu and Warren Pear (Univ. Pennsylvania). Sequences encoding p21, p27, full length PU.1 or the PU.1-ets DNA binding domain (amino acids 159-262) were then cloned by PCR and inserted into these empty vector constructs upstream of the IRES using the restriction enzymes BglII and EcoRI (New England Biolabs). A list of constructs used for this study is provided in Table S2. The small molecule CDK4/6 inhibitor PD0332991 (Selleck Chemicals, Houston, TX) was added to culture medium at a concentration of 2.1 μM in 0.02% DMSO. The same concentration of DMSO added in the absence of inhibitor did not affect our experiments (data not shown).

Retroviral transduction

Viral particles were generated by transient co-transfection of the Phoenix-Eco packaging cell line with the retroviral construct and the pCL-Eco plasmid (Imgenex, San Diego, CA). Viral supernatants were harvested at two and three days after transfection, and immediately frozen at -80^{o}C until use. For retroviral transduction, tissue culture plates (Costar, Corning) were incubated overnight with 33 μg/mL retronectin (Clontech), and then loaded with viral supernatant. Cells were then cultured directly on virus-bound plates under the conditions described below.

Purification and sorting of fetal liver progenitors

Purification of fetal liver progenitors from PU.1-GFP mice was performed as previously described (*35*) . Briefly, E13.5 fetal livers were dissected from the fetuses of pregnant mice. Single-cell suspensions of fetal liver cells were then prepared, stained for lineage markers using biotin-conjugated lineage antibodies (Ter119, F4/80, Gr-1, CD11c, NK1.1, CD19), incubated with streptavidin-coated magnetic beads (Miltenyi Biotec), and passed through a magnetic column (Miltenyi Biotec). Lineage-depleted (Lin-) cells were eluted and stored in liquid nitrogen in freezing media (50% FBS, 40% αMEM, 10% DMSO) for future use. We did not observe any significant differences between fresh and previously-frozen Lin- cells with respect to their *in vitro* differentiation behavior. Frozen lineage-depleted fetal liver cells were either thawed and sorted immediately (Fig. S1, S2, S3, S10), or pre-cultured and concurrently infected with different retroviral constructs for two days prior to sorting (Fig. 1, 2, 3, S4, S5, S6, S7, S9, S12, S13, S14). Pre-culture/infection was performed on virus-bound plates (see above) using standard culture medium [80% αMEM (Gibco), 20% HyClone Fetal Bovine Serum (Thermo Scientific), Pen Strep Glutamine (Gibco), 50 μM β-Mercaptoethanol (Sigma)] supplemented with 5 ng/mL SCF, 5 ng/mL IL-7 and 5 ng/mL Flt3L (Table S3). Cells were then stained with cKit, CD27, a biotin-conjugated lineage

cocktail (Ter119, F4/80, Gr-1, CD11c, NK1.1, CD19), dye-conjugated-Streptavidin, and 7-aminoactinomycin D (7AAD, for some experiments, see Table S1), and were then sorted for fetal liver progenitors, defined as Lin- 7AAD- (when used) cKit+ CD27+PU.1-GFP-intermediate cells (Fig. S1). For some experiments (Fig. 2C-D, 3E, S5 and S12), this FLP population was further fractionated using the surface marker FcγR2/3. Cells transduced with retroviral constructs were sorted as mCherry+ cells to obtain infected fetal liver progenitors. For downstream culture experiments, the following populations were used: freshly-thawed and sorted FLPs (Fig. S1, S2, S3, S10); pre-cultured FLPs that were not infected (Fig. 1B-C, S4, S6); pre-cultured FLPs infected with MSCV-IRES-mCherry (Fig. 1D-H, 2, 3, S5, S7, S9, S12, S13, S14); pre-cultured FLPs infected with MSCV-PU.1-IRES-mCherry (Fig. 3, S13, S14); or pre-cultured FLPs infected with MSCV-PU.1-ets-IRES-mCherry (Fig. 2, S12). For experiments in Fig. 2B and S10, transduction of p21 and p27 was performed after sorting, by culturing on virus-bound plates. For imaging experiments, retrovirally-expressed mCherry served as a cell marker used for cell segmentation and tracking. For experiments using the CellTrace Violet cell proliferation dye (Invitrogen), sorted cells were then incubated with 5 μM CellTrace Violet at 37^{o}C for 10 minutes prior to culture. We note that fetal liver progenitors (Lin-cKit+CD27+) were chosen for these experiments as they express PU.1-GFP at uniform intermediate levels (Fig. 1, Fig. S1), rapidly differentiate into either B- or myeloid cells *in vitro* (*35*), and form B- or myeloid progeny with comparable frequencies in single-cell cloning experiments (Fig. S2).

Cell culture

Sorted FLPs were cultured either on tissue-culture treated plates (Costar, Corning) or on glass-bottom plates for imaging (Mattek, Ashland, MA). For imaging experiments (Fig. 1C-H, Fig. 3B-D), glass-bottom 96-well plates were coated with retronectin (40 μg/mL, Clontech) to promote cell adhesion. Cultured cells for imaging were plated at a density of 1200-1800 / well. This density was chosen to maximize the starting number of imaged cells (~20-30) while maintaining the culture at low enough cell densities for single-cells to be resolved continuously for four days. For experiments where sorted FLPs were subsequently transduced with retroviral constructs, cells were cultured directly on virus-bound plates, prepared as described above. Unless otherwise indicated, cells were cultured in standard medium [80% αMEM (Gibco), 20% HyClone Fetal Bovine Serum (Thermo Scientific), Pen Strep Glutamine (Gibco), 50 μM β-Mercaptoethanol (Sigma)] supplemented with 5 ng/mL SCF, 0.1 ng/mL IL-3, 5 ng/mL IL-7 and 5 ng/mL Flt3L (Table S3), except for experiments shown in Figs. 1, S4, S6, where 0.5 ng/mL or 5 ng/mL M-CSF was also added to promote macrophage differentiation. The low IL-3 concentrations used here facilitated survival of progenitors without excessively suppressing differentiation into the B-cell lineage (Fig. S2).

Flow cytometry of cultured cells

For flow cytometric analysis, cultured cells were then disaggregated, re-suspended in Fc blocking supernatant (2.4G2 hybridoma supernatant, prepared in the Rothenberg lab), then stained using the indicated antibodies (Table S1). Stained samples were then re-suspended, filtered through a nylon mesh to remove clumps, and analyzed using either a MacsQuant flow cytometer, or a MacsQuant VYB flow cytometer for mCherry-containing samples (Miltenyi Biotec, Auburn, CA). Acquired flow cytometry data was then analyzed using FlowJo flow cytometry analysis software (Tree Star Inc., Ashland, OR).

Timelapse imaging

Timelapse imaging of cultured cells was performed on a motorized inverted fluorescence microscope (IX-81, Olympus) using a 60x 1.4 NA oil objective (Fig. S7A). The microscope was fitted with laser-based

focus drift correction (ZDC, Olympus) to maintain a constant plane of imaging, and also fitted with a custom-built incubator to maintain a constant humidified environment at 37^{o}C with 7% CO_2. Images of cultured cells were acquired at fixed time intervals in the differential interference contrast (DIC) brightfield channel, and GFP and mCherry fluorescence channels using image acquisition software (Metamorph, Molecular Devices). Shorter timelapse intervals (3 minutes) were used for acquisition of DIC images to facilitate cell tracking, whereas longer timelapse intervals (15 minutes) were used for acquisition of GFP and mCherry images to minimize photo-toxicity and photo-bleaching. For each time point, images of overlapping adjacent fields of view were acquired by moving a motorized stage (Applied Scientific Instrumentation, Eugene, OR) in order to generate a larger tiled image of the cell culture (Fig. 1 – one 5 x 5 tile; Fig. 3 – two 4 x 4 tiles of different culture wells corresponding to EV and PU.1-transduced progenitors). This image tiling was performed so that the cells, which moved rapidly in culture, could be tracked for longer periods of time before escaping observation. Timelapse imaging was performed continuously for four days.

In order to generate the correction matrix for uneven fluorescence illumination (Fig. S7B), tiled images of uniformly fluorescent beads (Tetraspeck beads, Invitrogen) were acquired in the same fluorescence channels as those used for imaging at the same magnification. Images were then processed as described below.

Cell segmentation and tracking

Cell segmentation and tracking was performed using conventional algorithms and procedures for analysis of timelapse fluorescence images of living cells [for a review, see (*36*)]. These algorithms were implemented using custom-written code in MATLAB (Mathworks, Natick, MA) following this workflow:

(I) *Fluorescence image background-subtraction and illumination-correction.*
Background grayscale values were subtracted from each fluorescence image using a top-hat transform using a disk-shaped structuring element with radius larger than that of a cell. Background-subtracted images were then divided by the correction matrix for the same fluorescence channel. To generate the correction matrix, images of fluorescent beads were background-subtracted using the top-hat transform, and segmented by thresholding using Otsu's method. The integrated grayscale intensities, along with *x* and *y* coordinate positions for all segmented beads were then used to fit a second-degree polynomial surface (Fig. S7B). Interpolated values of this surface at pixel locations were then used for the correction matrix.

(II) *Automatic cell segmentation using an edge-detection based method*
Cells were segmented an image processing routine that combines edge detection of cell boundaries with morphological image processing routines to correct for segmented image defects (*37*). Corrected mCherry fluorescence images were smoothed using a Gaussian filter, then transformed using a 2-dimensional Laplacian filter to generate contrast at cell edges. Edges were then segmented by thresholding on negative values of this image. Small features in this edge-detected image were then removed using morphological erosion, and cell boundaries were filled to give rise to solid segmentable objects. Segmented objects were then enriched for cell-like objects based using selection on size, and eccentricity and integrated mCherry fluorescence intensity. These cell segmentations were then used to calculate integrated GFP fluorescence intensity, using corrected GFP fluorescence images generated in Step (I). We note that cells touching each other were sometimes segmented as a single object; these cells were re-segmented during manual cell tracking in step (V). Segmented cells were either then tracked (Steps III-VI) or subject to a cytometric analysis of the entire imaged cell population. For the latter, live-cells were first identified by gating

on mCherry versus object area axis, and then plotted as two-dimensional histograms of PU.1-GFP levels against time (Fig. 1E, 3B).

(III) *Automated cell tracking*. As a first pass, single-cell traces were inferred automatically from segmented cells using a least-squares optimization approach to minimize dissimilarity between cell pairs in adjacent images (*38*). Least-squares optimization was performed using the Munkres assignment algorithm to match nearby cells in adjacent fluorescence frames with each other. In implementing this algorithm, we also took into account similarities in cell area, and also in mCherry and GFP fluorescence intensities. The objective function *E* to be minimized is:

$$E = \sum w_{ij}$$

where the matrix element:

$$w_{ij} = [(x_i - x_j)^2 + (y_i - y_j)^2]^{0.5}/C_{dist} + |A_i - A_j|/(A_j C_{area}) + |G_i - G_j|/(G_j C_{GFP}) + |R_i - R_j|/(R_j C_{mCherry}).$$

and the summation is over all terms in the matrix. Here matrix elements *i* and *j* give the indices of segmented cell objects for two successive mCherry fluorescence frames. The first term on the right hand side corresponds to the Euclidean distance between the two objects *i* and *j*; the second, third and fourth terms correspond to the fold change in cell area, GFP integrated fluorescence intensity, and mCherry integrated fluorescence intensity. The weighting values *C* give the cutoff values for these different parameters. If any of these terms exceed unity, the matrix element is set to infinity, forbidding an assignment between these two objects. This assignment algorithm was run for all pairs of successive mCherry fluorescence frames in timelapse image sequence to generate contiguous cell tracks. Cell objects that were not matched to other cells in a successive frame were carried over to be re-matched to the next frame, and this carry-over continued until the either the cell was matched, or if a maximum number of carry-overs was reached.

(IV) *Manual refinement of cell tracking*. Cell tracks generated using automated tracking (Step III) were then subject to manual refinement to correct assignment errors and omissions, label cell division events and death events and split touching cells. Individual cells were followed manually until they divided, died, exited from the field of view, or crossed paths with a nearby cell in a way that precluded unambiguous cell assignment between two successive frames. Cell death events were characterized by an abrupt loss in mCherry fluorescence, increase in cell granularity as observed in brightfield images, and cessation of cell movement for moving cells. To expedite manual segmentation and tracking, we developed a graphical user interface in MATLAB that allows the user to rapidly scroll through a timelapse movie, view multi-channel images with segmentation overlays, edit cell segmentations or assignments, and label cell division events (Fig. S7C).

(V) *Analysis of manually-refined cell tracks*. Manually-refined cell tracks were then used to generate individual cell lineage traces using a recursive graph-traversal algorithm. These cell lineages were then used for calculation of cell cycle lengths and promoter activities in different cell populations (Fig. 1F-H, 3C-D, S7E). For this analysis, single-cells were counted to fall within the defined population gates (Fig. 1D) only if more than 50% of the data points fell within the gate boundaries. Ancestors of macrophages (Mac early, Fig. 1H) were defined as cells with descendants that fell within the macrophage population gate, but were themselves outside the gate boundaries. For promoter activity calculations, time traces of PU.1-GFP levels for single cells over their entire observed lifetimes were fit to straight lines (Fig. S7E), and slopes of the linear fits, which give the rate of PU.1-GFP accumulation over time, were used as estimates of PU.1 promoter activity. For the mean cell cycle length for cells in a population, we used as an estimator the total number of observed frames for all cells in a given population divided by the total number of observed cell

division events in the population (Fig. 1H, 3D; see Fig. S18 for a graphical illustration). This estimator is not biased by the rapid and entry and exit of cells out of the imaging field of view (without observed cell division), and also to take into account cells with long cell cycles that were not observed to divide. To generate 95% confidence intervals for this mean cell cycle length estimate (Fig. 1H, 3D), a bootstrap method was used, where cells in a given population were randomly sampled with replacement to generate cell populations for calculating the distribution of mean cell cycle lengths.

All code is available from H.Y.K. (kueh@caltech.edu) upon request.

Measurement of PU.1 protein stability

For measurements of PU.1 protein stability (Fig. S6), macrophages derived from cultured FLPs were treated with 0.7 μg/mL cycloheximide (Sigma) for different periods of time (0-9 hours), then stained for PU.1 protein using the procedure described below. We note that higher concentrations of cycloheximide induced significant cell death within the observation time window, precluding measurement of PU.1 protein levels.

Immunofluorescence staining of PU.1 protein

For PU.1 immunofluorescence staining (Fig. S3, S6, S10), cells were fixed and permeabilized using the BD Cytofix/Cytoperm kit (BD BioSciences, San Jose, CA) and stained overnight in 5 μg/mL antibody at 4^{o}C. PU.1 levels were then measured using flow cytometry, or by fluorescence microscopy. For cells analyzed using fluorescence microscopy, cell nuclei were identified by co-staining with Vybrant DyeCycle Violet (Invitrogen) and used for segmentation in acquired images.

Gene expression analysis using quantitative RT-PCR

Total RNA was extracted from EV or PU.1-transduced cells using the RNeasy RNA isolation kit (Qiagen) and reverse transcribed into cDNA (SuperScript RT III, Invitrogen). cDNA from different samples were then mixed with the appropriate gene-specific primers (Table S4) and a quantitative PCR master mix reagent (SYBR GreenER, Invitrogen), and run on a real-time PCR machine (7900HT, Applied BioSystems). Reactions were run in triplicate, and relative expression levels were calculated based on median expression values of two biological replicates, using β-actin as a normalization control. Primers for a number of genes were designed with the aid of an online tool (*39*).

Mathematical Appendix

Here, we analyze a stochastic single-cell model of a positive feedback loop between PU.1 and the cell cycle, as experimentally observed. We show that this circuit architecture can by itself maintain two stable steady-states: a slow-dividing differentiated state with high levels of PU.1, and a fast-dividing progenitor state with lower levels of PU.1, in agreement with the observed PU.1 and cell cycle regulation in developing macrophages. We next compare the performance of this cell-cycle coupled feedback loop to that of a simple transcriptional positive feedback loop using the framework of mathematically-controlled comparisons, as developed by Savageau [45]. In this methodology, models representing alternate circuit architectures are constrained to be as similar as possible (see below), and are evaluated using defined performance objectives. We show that, for the parameters examined, cell-cycle coupled feedback enables cells to persist in a slow-dividing state for longer periods of time when gene expression is noisy. Finally, we consider a hybrid circuit containing both transcriptional and cell-cycle coupled feedback loops, and show that it can generate three stable steady-states that recapitulate PU.1 levels and cell cycle lengths for the observed pro-B, progenitor and macrophage populations respectively.

1. Model of a cell-cycle coupled feedback loop

In this model of positive feedback between PU.1 and the cell cycle, transcription and translation, together with mRNA and protein degradation, are described by first-order chemical reactions[1](Fig. S15A, left):

reaction	**rate**	
$m \rightarrow m+1$	$\alpha_m V(t)$	(1)
$m \rightarrow m-1$	$\delta_m m$	(2)
$p \rightarrow p+1$	$\alpha_p m$	(3)
$p \rightarrow p-1$	$\delta_p p.$	(4)

[1]Here, transcription, translation, as well as mRNA and protein degradation are approximated using simple first-order chemical kinetics; while the detailed kinetics of these processes are more complex in cells, our subsequent analysis, together with existing theory [46] will show that our conclusions hold independent of the exact kinetic form of these processes.

Here m and p denote PU.1 mRNA and protein copy numbers, and $V(t)$ is the nuclear volume, given by:

$$V(t) = V_0 \qquad \text{if } t < \tau_1 \tag{5}$$

$$= V_0[1 + (t - \tau_1)/\tau_2] \qquad \text{if } \tau_1 < t < \tau_1 + \tau_2 \tag{6}$$

Here τ_1 is the duration of the G1 phase of the cell cycle, and τ_2 is the combined duration of the S, G2 and M phase. The beginning of the cell cycle is taken to be $t = 0$. Here, nuclear volume remains constant at V_0 during G1 and increases linearly to twice its initial volume during the combined S-G2-M phase (Fig. S15A, center). Note here that mRNA transcription scales with nuclear volume to account for the increase in DNA copy number during DNA synthesis. To model the inhibition of cell cycle progression by PU.1, we assume that PU.1 arrests cells at a G1 transition checkpoint above a threshold concentration, such that:

$$\tau_1 = \min\left[T, \tau_1^{\max}\right], \qquad \text{where} \tag{7}$$

$$T = \{t \mid (p(t)/V < \pi_c) \wedge (t > \tau_1^{\min})\}$$

Here $\tau_1^{\min}$ represents the time it takes for cells to reach the G1 transition checkpoint; release from this checkpoint either occurs immediately after PU.1 protein concentration falls below the critical value π_c (representing the minimum of the set of times T), or when a maximal time $\tau_1^{\max}$ is reached, whereby the G1 checkpoint is released by a PU.1-independent mechanism (Fig. S15A, right). In this model, cells progress immediately to S phase, and the combined time of the S-G2-M phase τ_2 is taken to be constant. Finally, the cell divides at time $(\tau_1 + \tau_2)$, whereby PU.1 mRNA and protein are randomly partitioned between the two daughter cells following a binomial distribution. The reactions described here were simulated using the Gillespie algorithm [44], where cell cycle events (G1 checkpoint release and cell division) were executed concurrently with the stochastic simulations of mRNA and protein level changes. In these simulations, we chose kinetic parameters relevant to a mammalian cell context (Table S5).

From stochastic simulations, we found that this cell-cycle coupled positive feedback loop can generate two states that can persist over many cell cycles, a slow-dividing state with high PU.1 protein levels, and a fast-dividing state with low PU.1 protein levels (Fig. 4A). The system could switch spontaneously from a slow-dividing high PU.1 state to a fast-dividing low PU.1 state due to stochastic fluctuations in mRNA and protein levels (Fig. S15B), though, under the parameter

conditions examined, these switching events were rather infrequent (Fig. S15B, ∼1200 hours). These results indicate that a cell-cycle coupled feedback loop can by itself generate two stable states with different regulatory factor levels.

2. Iterative map analysis of the cell-cycle coupled feedback loop

How does a cell-cycle coupled feedback loop generate two stable-states, and how do these steady-states depend on parameter values? To answer this question, we develop an analytical framework for examining steady-state stability using iterative maps. First, define p_n to be the level of PU.1 protein at the beginning of the nth cell cycle. To gain analytical insight, we treat the problem deterministically, assuming that there exists a function that maps the level of PU.1 protein at the beginning of the $(n+1)$th cell cycle to that at the beginning of the nth cell cycle, as follows:

$$p_{n+1} = f(p_n) \tag{8}$$

To further simplify the problem, we take the limit where the protein is completely stable, such that it accumulates at a constant rate r over time[2]. These assumptions approximate our experimental measurements showing that PU.1 has a half-life of ~ 70 hours (Fig. S6). In this limit, the iterative function in (8) is given by:

$$\begin{aligned} f(p_n) &= \frac{r t_{\text{pro}} + p_n}{2} \qquad \text{if } p_n < p_{\text{crit}} \\ &= \frac{r t_{\text{mac}} + p_n}{2} \qquad \text{if } p_n > p_{\text{crit}}. \end{aligned} \tag{9}$$

Here, t_{pro} and $t_{\text{mac}} (> t_{\text{pro}})$ give the cell cycle lengths for progenitor and differentiated states, and p_{crit} is a critical level of p_n above which the system switches to a slow-dividing state. In this simple model, p_{crit} but will be slightly lower than $p_c = \pi_c V$, the threshold PU.1 level required for maintaining G1 checkpoint arrest (Eq. 7), as PU.1 protein levels will accumulate during G1; moreover, in this discrete model, we do not explicitly account for the different phases of the cell cycle but instead absorb their effective contributions into the reduced set of parameters described above.

[2]To calculate this iterative function for the general case where protein degradation is significant and synthesis rates are not necessarily constant, we can integrate the rate equations for gene expression over the length of a cell cycle using p_n as the initial protein level.

By plotting Eq. 9 against a straight line with slope unity, we can generate cobweb plots that demonstrate the existence of two stable steady-states, one with low PU.1 levels, and another with high PU.1 levels (Fig. S16). To solve for the steady-state of the system, we solve for $p_\infty = f(p_\infty)$. Two solutions are possible:

$$p_{\text{low}} = rt_{\text{pro}} \qquad \text{and} \qquad p_{\text{high}} = rt_{\text{mac}}. \tag{10}$$

From visualization of the phase plot in Fig. S16, the following parameter conditions for bistability emerge:

$$rt_{\text{pro}} < p_{\text{crit}} < rt_{\text{mac}}. \tag{11}$$

This states that the critical level of PU.1 protein required at the beginning of the cell-cycle for cell-cycle lengthening p_{crit} needs to fall between the projected low and high values for steady-state PU.1 levels. If p_{crit} does not fall within these bounds, then the iterative function (Eq. 9) will intersect with the straight line of slope unity only once, giving rise to one stable steady-state.

3. Mathematically-controlled comparison of a cell-cycle coupled feedback with an alternate circuit architecture

What are possible selective advantages to utilizing cell-cycle coupled feedback loop involving PU.1 to maintain a slow-dividing differentiated state? Potential insights into this question can be gained by using the technique of mathematically controlled comparisons [45] to compare the cell-cycle coupled feedback loop to alternative circuit architectures that can also generate bistability and maintain a slow-dividing differentiated cell state. In this method, models from alternative designs are constrained to be as similar as possible, and then evaluated according to defined performance criteria. This method allows for fair comparisons of alternate circuit designs and is thus likened to a well-controlled competition experiment [45].

Here, we use mathematically-controlled comparison to compare the cell-cycle coupled feedback loop described above to a hypothetical transcriptional positive feeedback circuit where PU.1 activates its own transcription. In this model, PU.1 also inhibits the G1 to S transition above a threshold level, causing cell-cycle arrest in differentiated cells, but is instead maintained at two different steady-state levels through the transcriptional auto-regulatory loop (Fig. S17A, right). We chose this circuit architecture for this comparison as it represents a minimal pure transcriptional

feedback that supports a slow-dividing differentiated state; our results here do not rule out the existence of other circuit transcriptional feedback architectures that may match or out-perform the cell-cycle coupled feedback loop according to the defined performance objectives.

Transcriptional feedback model

The equations describing the transcriptional feedback loop are the same to that for the cell-cycle coupled feedback loop (Eq. 1-7), except that we modify the mRNA synthesis rate to incorporate positive feedback, as follows:

reaction	**rate**	
$m \rightarrow m+1$	$\alpha_m^{(1)} V$	if $p/V \leq \pi_t$
	$\alpha_m^{(2)} V$	if $p/V > \pi_t$

(12)

where $\alpha_m^{(1)} < \alpha_m^{(2)}$. Here we have modeled the dependence of PU.1 transcription rate on nuclear PU.1 concentration by a step function, assuming a highly-cooperative response of the PU.1 promoter to levels of PU.1. It is also possible to model positive transcriptional feedback using other transfer functions, and our subsequent study of the hybrid feedback loop will utilize a Hill function to model positive feedback (see below); however, we have chosen here a step-function for transcriptional activation, as it provides a direct comparison with the threshold for PU.1-mediated cell-cycle arrest, which also implies a step-like change in control of cell division rate. Our subsequent analysis of this system will show that our main conclusions do not depend on the exact functional form of positive feedback.

An important difference between the cell-cycle coupled feedback and transcriptional feedback models lies in the magnitude of rate of protein degradation, given by δ_p in the models. For the cell-cycle coupled feedback loop, the PU.1 protein degradation rate must be small compared to the rate of progenitor cell division:

$$\delta_p < (\tau_1^{\min} + \tau_2)^{-1} \tag{13}$$

Because PU.1 protein is stable, it can accumulate as a result of cell-cycle lengthening, thus allowing the cell-cycle coupled positive feedback loop to be closed (Fig. S17A, left). In contrast, for the transcriptional positive feedback loop, the PU.1 protein degradation rate must be set to be larger

than the progenitor cell division rate:

$$\delta_p > (\tau_1^{\min} + \tau_2)^{-1} \tag{14}$$

The faster degradation rate prevents PU.1 protein from accumulating as a result of cell-cycle lengthening, and render's PU.1's effective degradation independent of the cell cycle length. This ensures that, for the purposes of this comparison, positive feedback occurs exclusively through transcriptional PU.1 auto-regulation and not through cell-cycle mediated PU.1 accumulation. As we will see, this difference in protein stabilities between these two models will provide the key difference in the performances of the two models. It is possible to envision models where PU.1 protein is stable, and thus both transcriptional and cell-cycle coupled feedback models are operational at the same time; the functional properties of such hybrid feedback models will be interesting to study, and we analyze one instance of such a hybrid feedback model in the context of PU.1 regulation in pro-B cells, progenitors and macrophages (see below, and Fig. 4B-C). However, in order to clearly characterize the differences in the functional properties between the two circuit architectures, we perform this comparison using a regime of this extended model where only the transcriptional feedback loop is active.

Constraints on the two models

To enable a mathematically-controlled comparison of the cell-cycle coupled feedback loop with the transcriptional feedback loop, it is necessary to constrain the parameter values of these two models such that they are as similar as possible. As a starting point for this comparison, we adopted the parameters we used for the cell-cycle coupled feedback loop simulations (Fig. S15), and chose parameters of the transcriptional feedback model such that the following constraints were met:

1. Both models generate a slow-dividing high-PU.1 state, and a fast-dividing low-PU.1 state.

2. The average steady-state PU.1 protein levels in the high-PU.1 and low-PU.1 states are the same for both models.

3. The cell cycle lengths in the high-PU.1 and low PU.1 states are the same for both models.

4. Both models have the same mRNA transcription and degradation rates in the high-PU.1 state. This ensures that both models have similar mRNA fluctuations in the slow-dividing

high PU.1 state[3].

5. Both models have the same critical PU.1 concentration for G1/S arrest (π_c); furthermore, the critical PU.1 concentration for transcriptional activation in the transcriptional feedback model (π_t, Eq. 12) is also set to the same value. This choice of PU.1 threshold levels equalizes the extent of the basins of attraction for both models.

After implementation of these constraints for the transcriptional feedback loop model, there remains one free variable, as translation rate α_p and protein degradation rate δ_p can still vary but are constrained to have the same ratio C. Here, we will perform the comparison using one fixed value of (α_p, δ_p), where δ_p is much larger than the cell division rate for the transcriptional feedback loop, as discussed above. For a more exhaustive comparison, one can simulate the model for different parameter values satisfying the relation $\alpha_p/\delta_p = C$ within the bounds specified by Eq. 14; however, our subsequent analysis will show that this is not necessary, as the main results of this model do not depend on the exact values chosen for these parameters.

Performance objectives

In choosing an performance criterion with which to compare these two systems, we surmised that maintaining a stable slow-dividing differentiated state amid noisy gene expression may be an important functional objective of the system, as failure to do so can result in a differentiation arrest and leukemic transformation [16-19]. Therefore, we used as a performance criterion the average time of spontaneous switching from the slow-cycling high-PU.1 (differentiated) state to the fast-cycling low-PU.1 (progenitor) state.

Results and analysis

Here, we simulated both feedback loop models using parameters fixed by the constraints described above (see Table S5). We started these simulations at $t = 0$ in the slow-dividing high-PU.1 state,

[3]By model construction, the transcriptional feedback model will also have lower mRNA transcription rates in the low-PU.1 state, in contrast to the cell-cycle coupled feedback model, where mRNA transcription rates are constant. This may affect the stability of the low-PU.1 (B-cell potentiating) state, although that is not investigated here in detail; instead, to investigate the basis for macrophage developmental stability, we examine only the switch from the high PU.1 state to the low PU.1 state, which is not affected by PU.1 mRNA levels in the low PU.1 state.

and then measured the time it took for the system to spontaneously switch to the fast-dividing low-PU.1 state. These simulations showed that the transcriptional feedback loop can also generate a slow-dividing PU.1-high state and a fast-dividing PU.1-low state (Fig. S17B). Cell-cycle lengths, PU.1 protein levels, as well as PU.1 mRNA levels in the PU.1-high state were very similar to those obtained for the cell-cycle coupled feedback loop (Fig. S17B, left versus right). However, we found that the slow-dividing state generated by transcriptional feedback switched spontaneously to a fast-dividing progenitor state more rapidly (Fig. S17B, right), indicating that this slow-dividing state is less stable than the one maintained by cell-cycle coupled feedback. To further test this idea, we repeated these simulations one hundred times for each model, and used this data to calculate the percentage of cells persisting in the high-PU.1 slow-dividing state as a function of time (Fig. S17C). For the cell-cycle coupled feedback model, we found that most cells ($> 90\%$) maintained the slow-dividing high-PU.1 state for over 200 hours, or 4 macrophage cell cycles (Fig. S17C, solid lines); in contrast, for the transcriptional feedback model, almost all cells ($> 90\%$) had already switched to the fast-dividing low-PU.1 state within 200 hours (Fig. S17C, dotted lines). This result indicates that the slow-dividing high-PU.1 state maintained by the cell-cycle coupled feedback loop persists over considerably longer periods of time compared to the corresponding state for the transcriptional positive feedback loop, under the constrained parameter conditions of these simulations.

The cause of these differences in steady-state stability between the two models can be seen from an examination of the PU.1 mRNA and protein time traces for the two models (Fig. S17B). For both feedback models, mRNA levels fluctuated rapidly due to stochastic mRNA synthesis and degradation, and the magnitude of these fluctuations were similar (Fig. S17B, top); however, PU.1 protein level fluctuations were considerably faster and larger in amplitude for the transcriptional feedback loop compared to the cell-cycle coupled feedback loop (Fig. S17B, middle). These larger and more frequent fluctuations in PU.1 protein levels for the transcriptional positive feedback loop increases the rate at which PU.1 levels spontaneously fall below the critical threshold for mediating cell-cycle arrest (Fig. S17B, dotted line). In contrast, PU.1 protein levels accumulated more steadily for the cell-cycle coupled feedback loop, despite the fluctuations in mRNA levels.

Insights into the generality of the differences in steady-state stability between these two models can be obtained by examining analytical expressions for the expected magnitude and frequency of protein fluctuations for the stochastic gene expression model utilized here (Eq. 1-4). From previous

work [46], we know that the relative magnitude of protein level fluctuations is given by:

$$\frac{\sigma_p^2}{\langle p \rangle^2} = \frac{1}{\langle p \rangle} + \frac{1}{\langle m \rangle} \cdot \frac{\delta_p}{\delta_p + \delta_m} \tag{15}$$

where the average mRNA and protein levels at steady-state are:

$$\langle m \rangle = \frac{\alpha_m}{\delta_m} \tag{16}$$

and

$$\langle p \rangle = \frac{\alpha_p \alpha_m}{\delta_m \delta_p} \tag{17}$$

respectively[4]. In our comparison, both models are constrained to have the same average protein levels $\langle p \rangle$, mRNA levels $\langle m \rangle$, as well as mRNA degradation rate δ_m. However, the protein degradation rate δ_p differs significantly for the two models; the protein degradation rate for the cell-cycle coupled feedback loop is much lower than that for the transcriptional positive feedback loop model (0.02 hr^{-1} versus 0.3 hr^{-1}), and is also considerably lower than the mRNA degradation rate (δ_m = 0.3 hr^{-1}). This lower protein degradation rate – a consequence of the long PU.1 protein half-life in the cell-cycle coupled feedback model – allows the system to time-average fluctuations in mRNA levels, thus reducing the contribution of mRNA fluctuations to the variability in protein levels (i.e. the second term on the right hand side of Eq. 15). From other work [46], we know that this time-averaging behavior of stable protein is a general property of a gene-expression system and is independent of the detailed kinetics of individual steps; hence, we expect our findings to also generalize to more models that consider in more intricate detail the processes of transcription, translation, and mRNA/protein degradation. Such time-averaging to maintain steady-state stability may be especially important for mammalian systems, where mRNA copy numbers are 2-4 orders of magnitude lower than protein copy numbers [24], such that the transcriptional noise term in Eq. 15 dominates. We note that, in this transcriptional-noise dominated regime, changes in average protein levels due to translational rate changes would be expected to have little effect on the relative magnitude of protein fluctuations; consistent with this assertion, simulations done with a tenfold reduction in both protein copy numbers (by translation rate reduction) and feedback activation thresholds gave rise to the same conclusions (data not shown).

[4]For simplicity, we have dropped the cell volume term in Eq.1, which is taken to be of order unity; this omission is not expected to affect our conclusions here.

To obtain the timescales of protein flutuations in the system, we can analyze a deterministic equivalent of this gene expression model, given by:

$$\frac{\mathrm{d}}{\mathrm{d}t}\begin{pmatrix} m-\langle m\rangle \\ p-\langle p\rangle \end{pmatrix} = \begin{pmatrix} -\delta_m & 0 \\ \alpha_p & -\delta_p \end{pmatrix}\begin{pmatrix} m-\langle m\rangle \\ p-\langle p\rangle \end{pmatrix} \tag{18}$$

From a solution of this linear system, we can show that the two characteristic timescales for protein levels are given by:

$$T_1 = 1/\delta_m \tag{19}$$

$$T_2 = 1/\delta_p. \tag{20}$$

As a result of the slower protein degradation rate δ_p, the cell-cycle coupled feedback loop has a considerably longer protein relaxation timescale $T_2(\gg T_1)$ compared to the transcriptional positive feedback loop, where mRNA and protein degradation rates are similar ($T_2 \sim T_1$). Consequently, protein levels will fluctuate about the average steady-state PU.1 value on a slower timescale. Taking these analytical results together with numerical simulations performed above, we conclude that the cell-cycle coupled feedback loop exhibits smaller and slower protein fluctuations than the transcriptional positive feedback loop, and consequently shows a significantly reduced rate of spontaneous switching between different steady states. This result suggests that the cell-cycle coupled feedback architecture more effectively maintains a stable growth-arrested state amid noisy gene expression, and could provide advantages compared to the transcriptional auto-regulatory circuit in systems when such stability is important.

4. Analysis of a hybrid feedback loop that generates three stable steady-states

We next consider a hybrid feedback model where PU.1 positively regulates itself, both through cell-cycle lenghtening, and also by transcriptional activation. We will show that this hybrid transcriptional/cell-cycle feedback architecture can give rise to three stable steady states corresponding to the pro-B, progenitor and macrophage populations respectively.

As with the transcriptional feedback loop analyzed above, the equations describing the hybrid feedback loop are the same as that for the cell-cycle coupled feedback loop (Eqs. 1-7), except with

the following modification of the mRNA synthesis rate:

$$\textbf{reaction} \qquad \textbf{rate} \tag{21}$$

$$m \to m+1 \qquad \left[\alpha_m^{(1)} + (\alpha_m^{(2)} - \alpha_m^{(1)}) \cdot \frac{(p/V)^N}{(p/V)^N + \pi_t^N}\right] V \tag{22}$$

Here mRNA production rate increases from a basal rate $\alpha_m^{(1)}$ to a maximal rate $\alpha_m^{(2)}$ with Hill coefficient N and a half-maximal activation PU.1 concentration of π_t. In choosing parameters for simulations, we utilized the same cell cycle parameters ($\tau_1^{\max}$, $\tau_1^{\min}$, V_0, π_c, τ_2), the same mRNA degradation rate (δ_m), as well as the same protein production and degradation rates (α_p, δ_p) as those for the cell-cycle coupled feedback loop (see Table S5). We set the maximal mRNA production rate ($\alpha_m^{(2)}$) to be the same as the constant mRNA production rate for the cell-cycle coupled feedback model (α_m). Furthermore, we assume the critical PU.1 concentration for half-maximal transcription activation π_t is considerably lower than that for PU.1-mediated G1 arrest π_c. This assumption is supported by our experimental findings that increasing PU.1 levels by retroviral transduction does not further activate endogneous PU.1 transcription (Fig. 3), whereas reducing PU.1 activity by dominant negative PU.1-ets does decrease PU.1-GFP expression (Fig. S12). Moreover, the existence of this transcriptional feedback loop is generally supported by other studies showing a role for positive feedback in the control of PU.1 transcription during lymphoid and myeloid development [7, 10-14].

In simulations with the parameters described above (see also Table S5), we found that this hybrid feedback loop can generate three stable states with PU.1 levels and cell cycle lengths that loosely correspond to those found in pro-B cells, progenitors and macrophages respectively (Fig. 4B). When started with different initial levels of PU.1 protein, the system can evolve into three distinct steady-states: 1) A fast-dividing state with low levels of PU.1 (Fig. 4B, red); 2) A fast-dividing state with intermediate levels of PU.1 (Fig. 4B, gray); 3) A slow-dividing state with high levels of PU.1 (Fig. 4B, blue). These cell division rates and PU.1 levels respectively correspond to those observed for the pro-B, progenitor and macrophage populations. Therefore, we propose that this hybrid feedback model may provide a basis for analyzing PU.1 regulation during the B-cell and macrophage fate determination.

5. Phase plane analysis of the different feedback architectures

To further understand how multiple stable states emerge from the cell-cycle coupled feedback loop and the hybrid feedback loop simulated above, we consider an alternate model description of these two feedback architectures, where stochastic effects are neglected and cell division rates are approximated by a continuous function. While this approach introduces further simplifications to the single-cell models above, it will allow us to use phase diagrams to visualize individual steady-states, providing insight into parameter requirements for multi-stability.

Based on the equations for the cell-cycle coupled feedback model (Eqs. 1-7) and the hybrid feedback model (Eq. 21), we formulate a simplified model where we use a single ordinary differential equation to describe the time evolution of PU.1 protein:

$$\frac{dp}{dt} = A(p) - \big[C(p) + D\big]p \tag{23}$$

where p is the level of PU.1, A is the rate of protein synthesis, C is the rate of cell division, and D is the rate of protein degradation. The synthesis rate is either constant for the cell-cycle coupled feedback model:

$$A(p) = A_0 \tag{24}$$

or

$$A(p) = A_{\min} + (A_{\max} - A_{\min}) \cdot \frac{p^M}{K_p^M + p^M} \tag{25}$$

for the hybrid feedback model. Here $A_{\min}$ and $A_{\max}$ are the basal and maximal rates of PU.1 synthesis, and K_p is the critical PU.1 level required for half-maximal activation of PU.1 transcription. For the both models, the rate of cell division is given by:

$$C(p) = C_{\min} + (C_{\max} - C_{\min}) \cdot \frac{K_c^N}{K_c^N + p^N} \tag{26}$$

where $C_{\max}$ and $C_{\min}$ are the maximal and minimal rates of cell division respectively. The cell division rate decreases when PU.1 levels increase, from an initial rate $C_{\max}$ in progenitors to a reduced rate $C_{\min}$ in differentiated cells. K_C gives the PU.1 level at which this decrease in cell division rate is half-maximal, and N gives the effective Hill coefficient for this decrease. Note that N need not be the same as M, the Hill coefficient for PU.1 transcriptional activation, as it will depend not only on PU.1/DNA interactions but also on the biochemistry of the PU.1 target proteins responsible for mediating G1 checkpoint arrest. In stochastic simulations, we effectively

consider the limit where $N \to \infty$, where PU.1 inhibits the G1 to S transition only above a certain threshold. Using these equations, we generated phase diagrams by plotting PU.1 synthesis and degradation rates against PU.1 levels, choosing parameters that loosely correspond to those used in single-cell simulations (Fig. 4C, see Table S6 for parameters). System steady-states are then given by intersections between these synthesis and degradation curves, and their stabilities can be determined by the relative heights of these two curves to the left or right of the intersection.

This analysis gives insights into how the cell-cycle coupled feedback loop and the hybrid feedback loop can generate two or three stable steady-states respectively. Due to a sharp decrease in the cell division rate (Fig. 4C, top), the PU.1 dilution rate becomes non-monotonic, bending back on itself to intersect the PU.1 synthesis curve three times (Fig. 4C, bottom). The outer two interections then correspond to the two stable steady-states (Fig. 4C, blue and gray circles), while the middle intersection represents an unstable steady-state that separates the basins of attraction for the two stable steady-states. This phase space structure can emerge in the cell-cycle coupled feedback loop, where synthesis rate is constant (Fig. 4C, gray), and also in the hybrid feedback loop, where synthesis rate increases with PU.1 levels (Fig. 4C, black).

When the rate of PU.1 synthesis increases cooperatively with PU.1 levels, as is the case for the hybrid feedback loop, the PU.1 synthesis curve can bend back to intersect the PU.1 dilution curve two more times. The lower intersection corresponds to an additional stable steady-state (Fig. 4C, red circle), and the higher intersection separates the basins of attraction for the two steady-states with low and intermediate PU.1 levels. This analysis shows that the hybrid feedback loop can generate three stable states with different PU.1 levels and cell division rates, as also shown with stochastic simulations (Fig. 4B). This analysis also reveals a model assumption that is critical for the generation of three stable states, namely that the critical PU.1 protein level for half-maximal activation of PU.1 transcription must be lower than that for half-maximal cell-cycle lengthening. In an alternative regime where the PU.1 thresholds for cell-cycle lengthening and transcriptional activation are similar, synthesis and degradation curves can only intersect with each other three times, giving rise to a maximum of two stable steady-states.

Supplementary Figure Legends

Fig. S1: Isolation of fetal liver progenitors (FLPs) from PU.1-GFP mice. Flow cytometry plots showing FLP sort gates (P0 – P4; Lin-7AAD-cKit+CD27+). Percentages give fraction of cells in the specified gate relative to that in parent gate. Histogram shows distributions of PU.1-GFP levels for the FLP population (P4) and in the parent population (P3). FLPs show a uniform level of PU.1-GFP.

Fig. S2: Fetal liver progenitors (Lin-cKit+CD27+) have B-cell and myeloid lineage potential. FLPs were sorted into individual wells, cultured for 7 days (5 ng/mL SCF, IL-7 and Flt3L +/- 0.5 ng/mL IL-3) and analyzed using flow cytometry. A) Flow cytometry plots showing surface CD19 (top) or CD11b (bottom) staining against PU.1-GFP for a starting culture with 100 cells (left), or for representative cultures of single-cells showing differentiation into B- (center) or myeloid (right) lineages. Cells shown here were cultured without IL-3. B) Single-cell B- or myeloid cell cloning frequencies of FLPs in cultures with or without 0.5 ng/mL IL-3. B-cells are defined as CD19+PU.1-GFP^{low} cells, whereas myeloid cells are defined as CD11b+PU.1-GFP^{high} cells. Concurrent differentiation into B- and myeloid lineages from a single-cell was not observed under these conditions. The addition of 0.5 ng/mL IL-3 promoted myeloid development at the expense of B-cell development. Note that lower concentrations of IL-3 (0.1 ng/mL) were used for the other experiments in the paper to allow concurrent observation of B- and myeloid development.

Fig. S3: Nuclear PU.1 protein levels vary linearly with PU.1-GFP levels. FLPs were cultured for 7 days and sorted for B-cells (CD19+PU.1-GFP-low), progenitors (Gr1-PU.1-GFP intermediate) and macrophages (PU.1-GFP high). Sorted cells were then stained for PU.1 protein using an A647-conjugated anti-PU.1 antibody, and analyzed using fluorescence microscopy. A) Fluorescence images showing DNA and PU.1 immunofluorescence staining for different sorted cell populations obtained after seven days in culture. Scale bar = 10 microns. B) Mean nuclear PU.1 levels plotted against mean PU.1-GFP levels for different sorted cell populations. Nuclear PU.1 levels were obtained by quantification of fluorescence images in A), whereas mean PU.1-GFP levels were obtained using flow cytometry. Data points give mean and S.E.M. for the different cell populations (B: *N*=235; Pro: *N*=72; Mac: *N*=108).

Fig. S4: Cultured FLPs develop into macrophages (CD11b+F4/80+Gr1-PU.1-GFP^{high}), granulocytes (CD11b+Gr1+F4/80-PU.1-GFP^{int}) and pro-B cells (CD19+PU.1-GFP^{low}) over time in a cytokine-dependent manner. Sorted FLPs were cultured in SCF, IL-3, FLt3L, IL-7 and M-CSF (or with components removed as indicated), and analyzed by flow cytometry. A) Histogram of PU.1-GFP levels (top), or flow cytometry plots of CD19, CD11b, F4/80 or Gr1 against PU.1-GFP levels for cells cultured for the indicated number of days in either complete cytokine cocktail (columns 1-3), or with a reduced cytokine cocktail missing the indicated components (columns 4-5). Bars define PU.1-GFP^{low}, PU.1-GFP^{int} and PU.1-GFP^{high} cell populations. Dotted lines show PU.1-GFP levels in input cells. B) Multi-parameter surface marker analysis of cell populations with different PU.1-GFP levels, as defined in A). Flow cytometry plots show CD19 versus CD11b levels (top), or F4/80 versus Gr1 levels for different CD19/CD11b sub-populations as defined by the indicated quadrants.

Fig. S5: Macrophage differentiation and PU.1-induced cell cycle lengthening occurs selectively in FcγR2/3^{low} FLPs, but not in FcγR2/3+ FLPs. A) Flow cytometry plots showing sort gates for the FcγR2/3+ and FcγR2/3^{low} FLPs (Lin-cKit+CD27+). Note that that FcγR2/3+ and FcγR2/3^{low} FLPs express PU.1-GFP at similar levels (right). B) FcγR2/3^{low} (left) and FcγR2/3+ (right) FLPs were cultured for 7 days in 5 ng/mL SCF, IL-7, Flt3L and 0.1 ng/mL IL-3, and analyzed by flow cytometry. Plots show CD11b against PU.1-GFP (top), and Gr1 against PU.1-GFP for the CD11b+ cells, gated as shown above. FcγR2/3^{low} FLPs give rise to

B-cells (PU.1-GFP low), macrophages and granulocytes, whereas FcγR2/3+ FLPs give rise to granulocytes but not macrophages and B-cells. C) EV or PU.1-transduced FcγR2/3^{low} or FcγR2/3+ FLPs were sorted, stained for CellTrace Violet, and cultured for 3 days in 5 ng/mL SCF, IL-7, Flt3L and 0.1 ng/mL IL-3. Flow cytometry plots show CD11b (top), Gr1 (middle) and CellTrace Violet (bottom) against PU.1-GFP levels for the different transduced cell populations. Histograms (bottom) compare CellTrace Violet levels for EV versus PU.1-transduced cells for either FcγR2/3^{low} FLPs (left) or FcγR2/3+ FLPs (right). Unstained controls (gray shaded) and initial CellTrace Violet levels at Day 0 (black) are also shown. Results indicate that retroviral of transduction of PU.1 induces cell-cycle lengthening in FcγR2/3^{low} FLPs but not in FcγR2/3+ FLPs. Data are representative of three independent experiments.

Fig. S6: PU.1 protein has a half-life that spans multiple progenitor cell cycle lengths. FcγR2/3^{low} FLPs were sorted, cultured in 5 ng/mL SCF, IL-7, Flt3L, M-CSF and 0.1 ng/mL IL-3 for 7 days, and then treated with 0.7 μM cycloheximide for the indicated amounts of time. In separate experiments (data not shown), we found that macrophages in culture are highly-sensitive to cycloheximide; by performing a titration, we determined this concentration of cycloheximide to be the maximal possible level that does not induce significant cell death, which confounds measurements. We note that this concentration of cycloheximide is still over a magnitude higher than its measured IC50 for inhibition of protein synthesis in cultured cells [~0.05 μM, from (*40*)]. Cells were then stained and analyzed by flow cytometry. A) Histograms show PU.1 protein levels in developing macrophages (CD11b+) before cycloheximide treatment (gray dotted), or after cycloheximide treatment for the indicated amounts of time (black). Background PU.1 staining levels in a pro-T cell line not expressing PU.1 (SCID.adh2C2) are shown in gray. B) Plots show mean PU.1 levels against elapsed time after CHX treatment for two independent experiments (left, right). Curves show best fit of the data to a single exponential of the form $f(t) = \exp(-t/\tau)$. Best-fit values for τ are shown. These results show that PU.1 has a half-life that is significantly longer than that of the progenitor cell cycle length (~10 hours), and can thus accumulate as a result of cell cycle lengthening.

Fig. S7: Experimental system for measuring PU.1-GFP levels and PU.1 synthesis rates in single cells using timelapse fluorescence microscopy. A) Schematic showing experimental parameters used for live-cell timelapse imaging. Timelapse intervals between successive images for the indicated channels are given by Δt; horizontal and vertical offsets for tiling image acquisition are given by Δx and Δy respectively. B) Surface plot showing the correction function for uneven GFP fluorescence illumination by the imaging setup. X- and Y- axes are measured in pixels. The correction function was measured experimentally by imaging uniformly-sized fluorescent microspheres separately for each wavelength (see Supplementary Methods). C) DIC (top), mCherry (middle) and GFP (bottom) images showing the segmentation and tracking of cells between two successive timelapse images (left and right). Yellow vertical and horizontal lines indicate the boundaries between adjacent tiled images along the x- and y-dimensions respectively. Colored boundaries in the mCherry and GFP channels represents cell segmentation, with each distinct color representing a distinct cell track. Numbers on the lower left give the elapsed time in hours; scale bar (lower right) represents 100 microns. D) Tree showing PU.1-GFP time traces for all cells tracked in a representative lineage. Filled area above each horizontal line gives PU.1-GFP levels in single cells over time. Branch points indicate cell division events, and termination of a cell trace reflects the exit of the cell from the imaging field of view. Horizontal scale bar gives PU.1-GFP levels (10^4 arbitrary units), and vertical scale bar gives time (10 hours). E) Plot showing PU.1-GFP levels against time for cells in the example lineage in D). Dots represent measured single-cell PU.1-GFP levels, and straight lines represent the best-fits by least-squares fitting. Each distinct color represents a distinct cell in the lineage. PU.1 promoter activity is given by the slope of the cells measured by least-squares fitting.

Fig. S8: GFP is photo-stable under timelapse imaging conditions. A T-cell lymphoma cell line (SCID.adh2C2) was infected with a GFP-expressing retrovirus (LZRS-GFP) and subject to timelapse imaging in the absence or presence of 10 μg/mL cycloheximide (CHX), a protein synthesis inhibitor. Imaging exposure conditions were similar to those shown in Fig. S7 (GFP channel exposure time – 800 ms, timelapse interval – 12 minutes, 60X 1.4 NA objective, ND2.0). GFP levels were tracked over time in single cells before (left) and after (center, right) addition of CHX. Time of CHX addition is given by vertical arrows (center, right). Straight lines represent best least-squares fit to the function $f(t) = A(1+kt)$; k represents the GFP accumulation rate (if positive) or the combined photobleaching/degradation rate (if negative). Values of k for GFP levels after CHX addition are much smaller than the cell division rate (~10^{-1}/hr), indicating that the half-life of fluorescing GFP greatly exceeds that of the cell cycle time under our imaging conditions.

Fig. S9: Representative lineage trees showing PU.1-GFP regulation in different cell populations. Trees show PU.1-GFP levels over time in single cell lineages within the following populations: Progenitors with high PU.1 promoter activity, Progenitors with low PU.1 promoter activity, Macrophages, and B-cells. Green shaded areas above branches represent single-cell PU.1-GFP levels, with vertical scale bar denoting 100,000 PU.1-GFP levels (arbitrary units). Horizontal direction represents time, with horizontal scale bar representing 20 hours. Asterisks indicate cell lineages in Fig. 1F. Red crosses indicate cell death events as seen by imaging. Cell death events were rare for the cells analyzed (4.0%, or 16 out of 403 cells were observed to die).

Fig. S10: Induced cell-cycle lengthening by CDK inhibitors p21 or p27 increases PU.1 protein levels. A)-B) Sorted FLPs were then cultured and concurrently transduced with empty vector, p21 or p27 retroviral constructs. Transduced cells were then re-sorted after four days for cells with different levels of PU.1-GFP, stained using an A647-conjugated αPU.1 antibody, and re-analyzed using flow cytometry. A) Histograms showing sort gates for transduced cell populations with low, intermediate and high PU.1-GFP levels. B) PU.1 protein (αPU.1-A647) against PU.1-GFP levels for EV (left), p21 (middle) and p27 (right) transduced cell populations with different PU.1-GFP levels. C) Median PU.1 protein levels against median PU.1-GFP levels obtained from flow cytometry plots in A). Data represent mean and standard deviation of two experiments.

Fig. S11: PU.1-ets blocks wildtype PU.1 function. A) Cartoon showing the domain organization of wildtype PU.1 and the PU.1-ets construct used in this study. The N-terminal trans-activation (TA) domain of PU.1 is enriched for aspartic acid (D), glutamic acid (E) and glutamine (Q) residues. B) Cells from a T-cell lymphoma cell line (Adh-2C2) were infected with various constructs as indicated on the top of each panel. After 48 hours, T-lineage cells were detected by CD25, and diversion to the myeloid lineage was determined by analyzing the surface up-regulation of the myeloid marker CD11b as described elsewhere (*41*). The data in the FACs-plots is representative of 2 independent experiments and shows that PU.1-ets effectively blocks myeloid diversion (CD25 down-regulation and CD11b up-regulation) by the wildtype PU.1 construct. C) PU.1-ets reduces the levels of known PU.1 positive target genes (*42*). E14.5 Bcl2-transgenic FLPs were cultured on Op9-DL1 for four days, transduced with empty vector (EV) control or PU.1-ets carrying retroviruses and sorted as infected DN2 (cKit+, CD44+, CD25+) cells. mRNA was enriched following total RNA extraction and used to build cDNA libraries which were sequenced using an Illumina HiSeq sequencer, essentially as described previously (*43*). Sequence reads were mapped to the NCBI mouse genome build (mm9) using Bowtie (http://bowtie-bio.sourceforge.net/index.shtml) and analyzed for differential expression using Cufflinks 2.0 (http://cufflinks.cbcb.umd.edu/). FPKM values for selected genes from 2 independent experiments

were normalized to their EV expression levels and the mean was plotted in the graph above. Error bars show one standard deviation. *indicates $p < 0.05$ using Student's *t*-test. The gene expression data shown in the bar chart is from another related study (Champhekar, A., Damle, S., Nutt, S.L., Carotta, S., Rothenberg, E.V., in preparation).

Fig S12: Inhibiting PU.1 activity using PU.1-ets promotes PU.1-GFP down-regulation, but does not accelerate pro-B cell formation. FcγR2/3^{low} FLPs transduced with either empty vector (EV) or the PU.1 Ets DNA binding domain (PU.1-ets) were sorted, cultured for 5 days in 5 ng/mL SCF, IL-7, Flt3L and 0.1 ng/mL IL-3 and analyzed. Flow cytometry plots (left) show CD19 (top) and CD11b (bottom) against PU.1-GFP levels for different transduced populations. Histograms (right) compare PU.1-GFP levels for EV versus PU.1-ets transduced cells. Data are representative of results from three independent experiments.

Fig. S13: **Exogenous PU.1 expression inhibits PU.1 down-regulation and CD19 up-regulation.** FLPs retrovirally transduced with either an empty vector (top) or PU.1 (bottom) were sorted, cultured for five days and analyzed using flow cytometry. Histogram (left) shows PU.1-GFP levels (left), and flow cytometry plots show CD11b against PU.1-GFP (center), or CD19 against PU.1-GFP (right). These plots show that PU.1-transduced FLPs give rise to lower percentages of PU.1-GFP low cells (left), and CD19-expressing cells (right). The CD19 fluorescent-conjugated antibody used here (CD19-e450, eBio1D3) gave considerably weaker staining than the one used in Figs. 1 and S4 (CD19-PE, 6D5), or the one used in Fig. S12 (CD19-PE, eBio1D3).

Fig. S14: Representative lineage trees comparing PU.1-GFP regulation in FLPs transduced with empty vector or PU.1. Trees show PU.1-GFP levels over time in single cell lineages for EV-transduced FLPs (top), and PU.1-transduced FLPs (bottom). Green shaded areas above branches represent single-cell PU.1-GFP levels, with vertical scale bar denoting 100,000 PU.1-GFP levels (arbitrary units). Horizontal direction represents time, with horizontal scale bar representing 40 hours. Dashed lines connecting the ancestors of each lineage indicate offset of initial observation from t = 0 hours. Asterisks indicate cell lineages in Fig. 3. Red crosses indicate cell death events. Cell death events were rare, and transduction with exogenous PU.1 did not increase the frequency of cell death for the cells analyzed (empty vector – 7.9%, or 12 out of 152 cells died; PU.1 – 3%, or 4 out of 133 cells died).

Fig. S15: Stochastic single-cell model of a cell-cycle coupled positive feedback loop. A) Description of model, with biochemical reactions for gene expression (left), cell-cycle dependent nuclear volume changes (middle), and different mechanisms for triggering G1/S checkpoint release (right). B) Results of a representative stochastic simulation run, showing the time evolution of PU.1 mRNA levels (top), protein levels (middle) and nuclear volume (bottom), along with corresponding histograms of PU.1 mRNA and protein copy numbers (left). Simulations were performed using the Gillespie algorithm (*44*). Here, the system was started at the slow-dividing high-PU.1 state to test whether this state could be maintained over many cell divisions. Model parameters are given in Table S5. Area shaded in yellow is magnified and shown as an inset on the right. In this simulation run, the system maintains a slow-dividing high PU.1 state for ~1200 hours, then switches spontaneously to the fast-dividing low PU.1 state. Threshold PU.1 level for cell-cycle arrest is indicated by the horizontal gray line (inset), whereas the time at which the G1/S transition is released during system switching is given by the vertical red line (inset). The same simulation run is shown again in Fig. S17B (left) for comparative purposes.

Fig. S16: Iterative map reveals bi-stability mediated by a cell-cycle coupled feedback loop. Iterative function (thick line) relates the initial protein levels after the *n*th cell division to initial protein levels after

the (*n*+1)th cell division. This function intersects twice with the straight line of slope unity (thin line), giving rise to two attractors (circles). Cobweb plots (dotted lines) show two sample trajectories with different initial starting conditions falling into the two different steady states. Arrows indicate direction of the system flows.

Fig. S17: A cell cycle-coupled feedback loop more effectively stabilizes a slow-dividing differentiated state compared to a pure transcriptional feedback loop. A) Model diagram for a cell-cycle coupled feedback loop (left), or a pure transcriptional feedback loop (right). Positive feedback loops are highlighted in blue, and spiral denotes the cell cycle. B) Time traces comparing the stability of a slow-dividing differentiated state maintained by either cell-cycle coupled feedback (left) or transcriptional feedback (right). Red line (right) indicates time of spontaneous reversion to a fast-dividing state for the transcriptional feedback loop model. C) Fraction of slow-dividing cells persisting as a function of elapsed time for either the cell-cycle coupled positive feedback model (solid line) or the transcriptional positive feedback model (dotted line). Simulation parameters are chosen to enable a mathematically-controlled comparison between the two models [(*45*), see Mathematical Appendix], and are given in Table S5.

Fig. S18: Method for unbiased estimation of cell cycle lengths in whole cell populations. Lineage trees show lifetimes of individual cells for two fictitious populations, A and B. Length along *x* axis is proportional to time. Vertical gray bars indicate beginning and end of observation window. Lines shaded with yellow indicate cells with completely-observed lifetimes (between two observed cell divisions). Red cross indicates observed cell death event. Estimator for mean cell cycle length of a cell population is given by the sum of observed lifetimes for all cells (with both complete and incomplete cell cycles), divided by the number of observed cells (i.e. $N_A = 15$ for population A, $N_B = 11$ for population B). In this example, accounting of only the cells with complete cell cycles (shaded yellow) will lead to a biased estimate of cell cycle length, as it will be influenced by differential kinetics of cell death and cell appearance/disappearance between the two populations, as well as truncated cell lifetimes due to finite window of observation. We note that this estimator is equivalent to the maximum likelihood estimator for the mean transition time of a first-order process that occurs at a constant fixed rate.

Figure S1

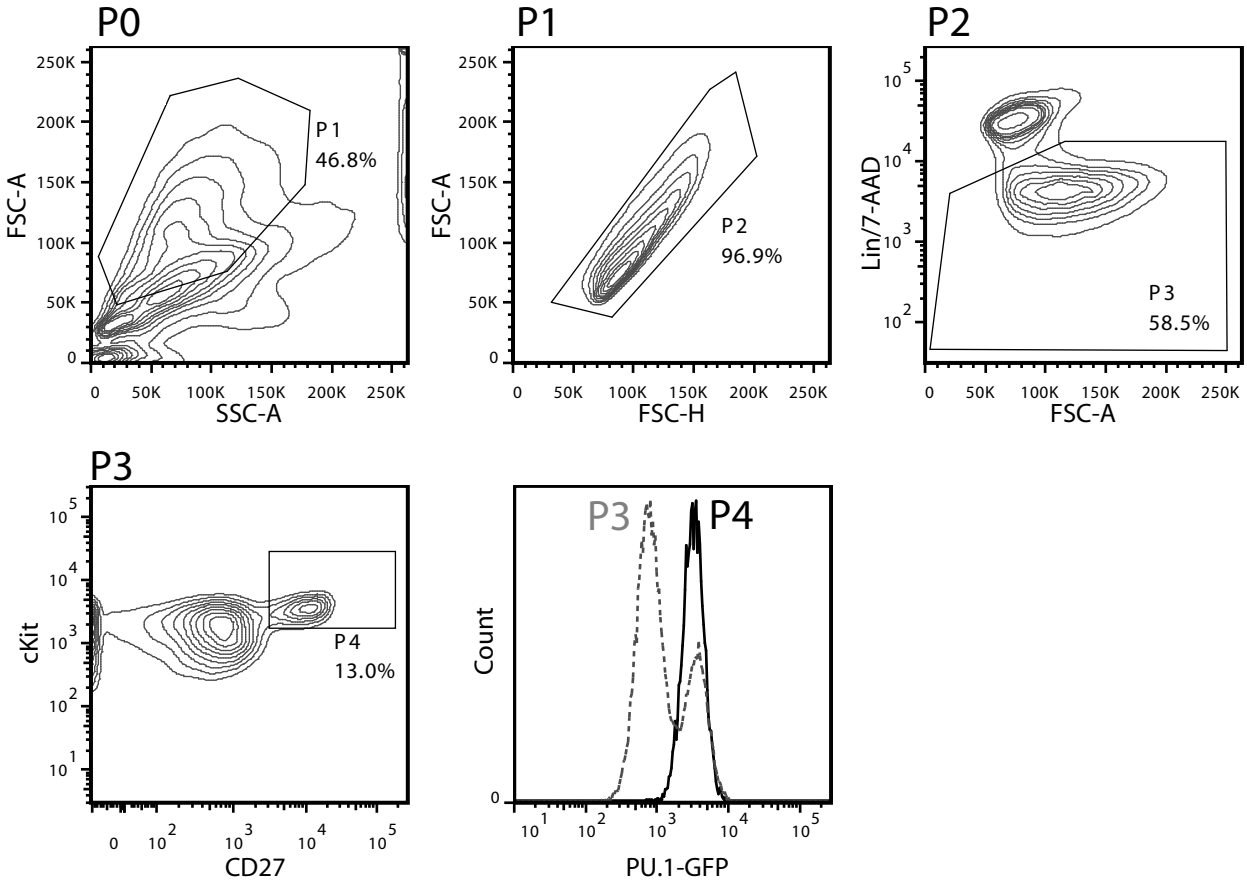
P0
FSC-A
SSC-A
P1
46.8%
P1
FSC-A
FSC-H
P2
96.9%
P2
Lin/7-AAD
FSC-A
P3
58.5%
P3
cKit
CD27
P4
13.0%
P3
P4
Count
PU.1-GFP

Figure S2

A)

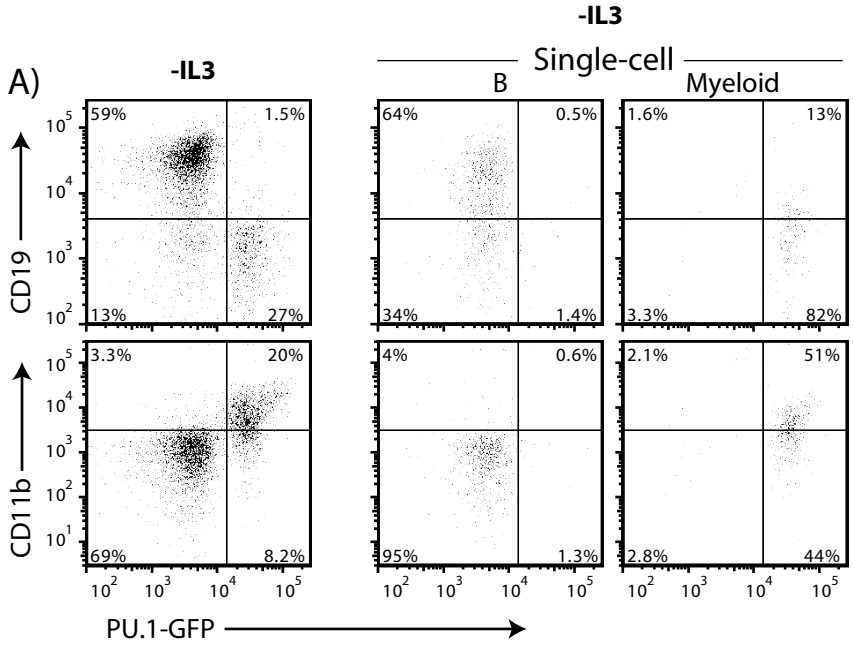

B)

	-IL3	**+IL3** (0.5 ng/mL)
B	9.5% (8/84)	3.2% (2/63)
M	10.7% (9/84)	23.8% (15/63)

Figure S3

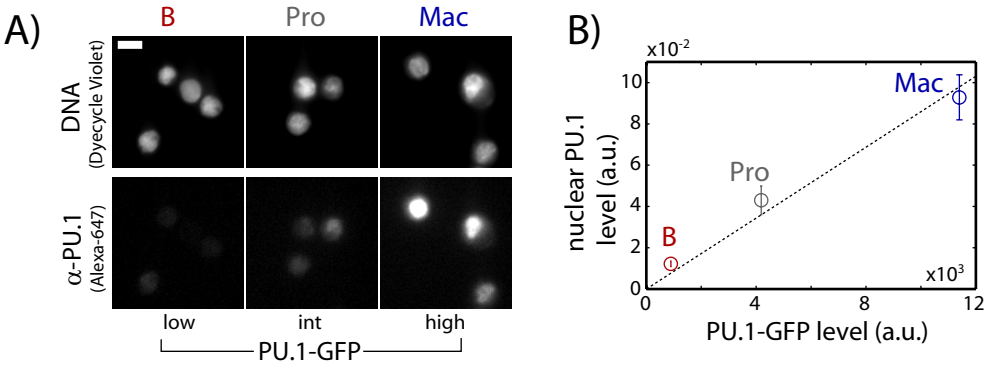
A)
B
Pro
Mac
DNA
(Dyecycle Violet)
α-PU.1
(Alexa-647)
low
int
high
PU.1-GFP
B)
x10-2
10
8
6
4
2
0
Mac
Pro
B
x103
0
4
8
12
nuclear PU.1
level (a.u.)
PU.1-GFP level (a.u.)

Figure S4

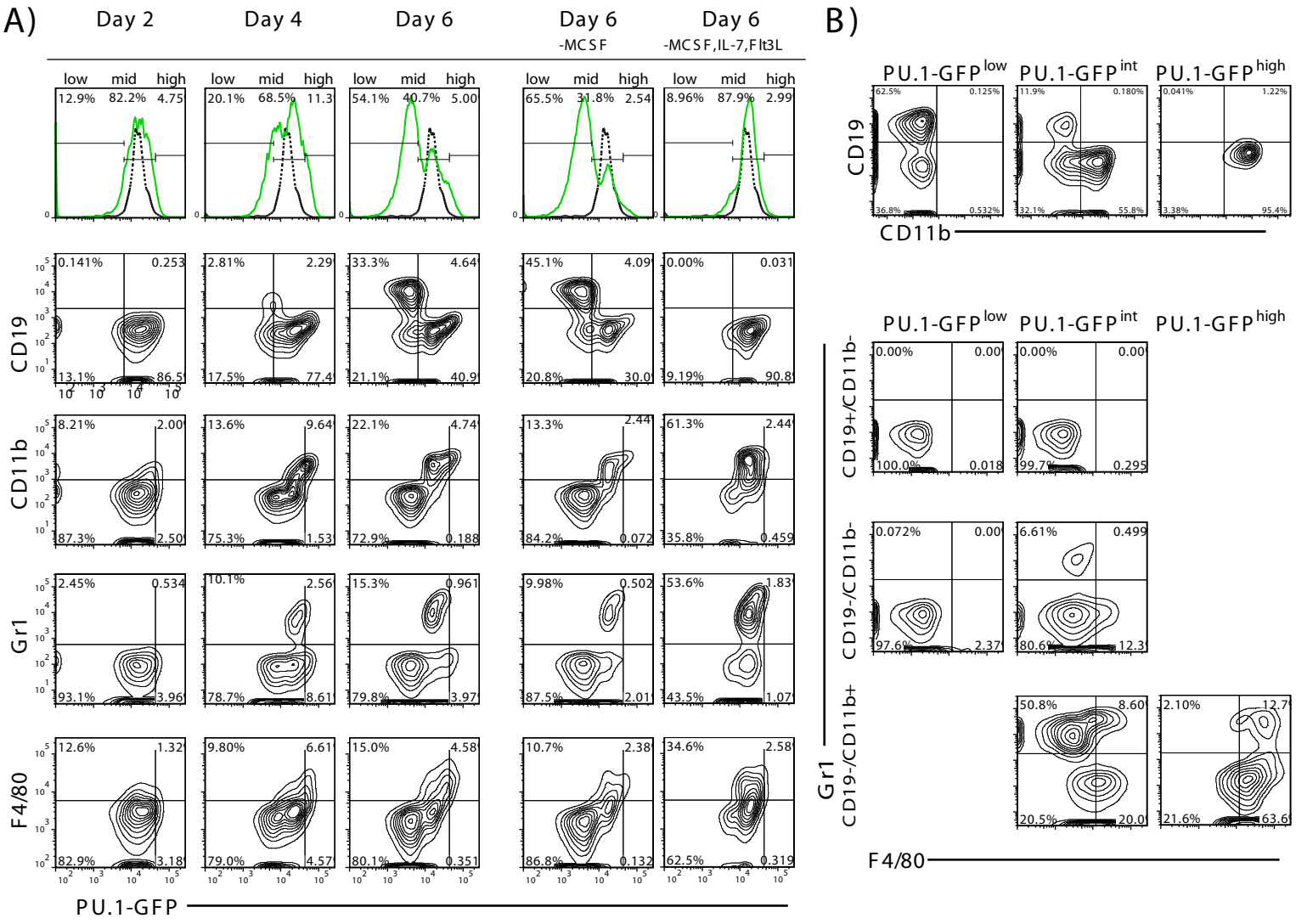
A)
Day 2
Day 4
Day 6
Day 6
-MCSF
Day 6
-MCSF,IL-7,Flt3L
low mid high
12.9% 82.2% 4.75
20.1% 68.5% 11.3
54.1% 40.7% 5.00
65.5% 31.8% 2.54
8.96% 87.9% 2.99
CD19
0.141% 0.253
13.1% 86.5
2.81% 2.29
17.5% 77.4
33.3% 4.64
21.1% 40.9
45.1% 4.09
20.8% 30.0
0.00% 0.031
9.19% 90.8
CD11b
8.21% 2.00
87.3% 2.50
13.6% 9.64
75.3% 1.53
22.1% 4.74
72.9% 0.188
13.3% 2.44
84.2% 0.072
61.3% 2.44
35.8% 0.459
Gr1
2.45% 0.534
93.1% 3.96
10.1% 2.56
78.7% 8.61
15.3% 0.961
79.8% 3.97
9.98% 0.502
87.5% 2.01
53.6% 1.83
43.5% 1.07
F4/80
12.6% 1.32
82.9% 3.18
9.80% 6.61
79.0% 4.57
15.0% 4.58
80.1% 0.351
10.7% 2.38
86.8% 0.132
34.6% 2.58
62.5% 0.319
PU.1-GFP
B)
PU.1-GFP low
PU.1-GFP int
PU.1-GFP high
CD19
62.5% 0.125%
36.8% 0.532%
11.9% 0.180%
32.1% 55.8%
0.041% 1.22%
3.38% 95.4%
CD11b
CD19+/CD11b-
0.00% 0.00
100.0% 0.018
0.00% 0.00
99.7% 0.295
CD19-/CD11b-
0.072% 0.00
97.6% 2.37
6.61% 0.499
80.6% 12.3
CD19-/CD11b+
50.8% 8.60
20.5% 20.0
2.10% 12.7
21.6% 63.6
Gr1
F4/80

Figure S5

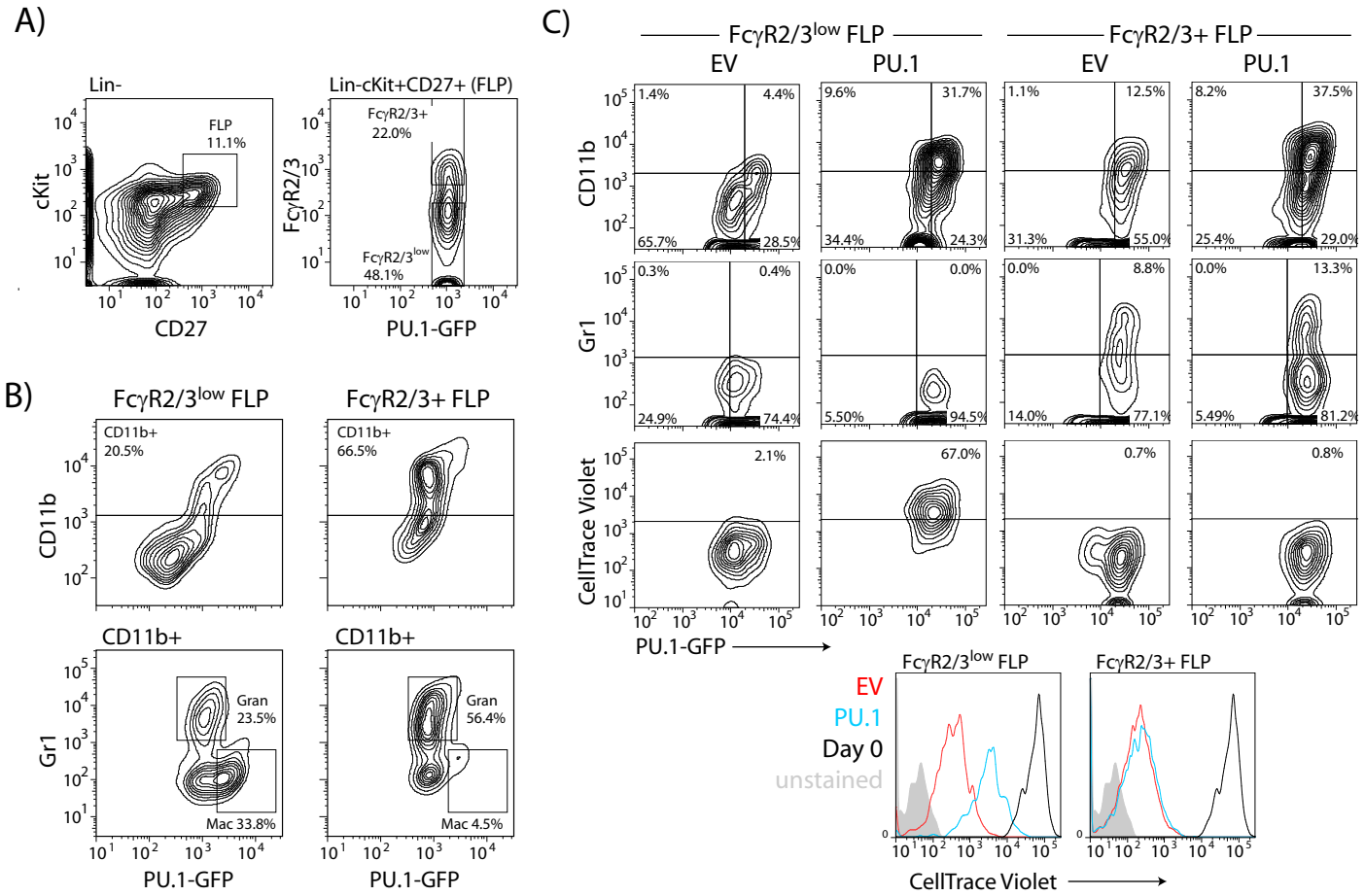
A)
Lin-
FLP
11.1%
cKit
CD27
Lin-cKit+CD27+ (FLP)
FcγR2/3+
22.0%
FcγR2/3low
48.1%
FcγR2/3
PU.1-GFP
B)
FcγR2/3low FLP
FcγR2/3+ FLP
CD11b+
20.5%
CD11b+
66.5%
CD11b
CD11b+
Gran
23.5%
Mac 33.8%
CD11b+
Gran
56.4%
Mac 4.5%
Gr1
PU.1-GFP
PU.1-GFP
C)
FcγR2/3low FLP
FcγR2/3+ FLP
EV
PU.1
EV
PU.1
1.4%
4.4%
65.7%
28.5%
9.6%
31.7%
34.4%
24.3%
1.1%
12.5%
31.3%
55.0%
8.2%
37.5%
25.4%
29.0%
CD11b
0.3%
0.4%
24.9%
74.4%
0.0%
0.0%
5.50%
94.5%
0.0%
8.8%
14.0%
77.1%
0.0%
13.3%
5.49%
81.2%
Gr1
2.1%
67.0%
0.7%
0.8%
CellTrace Violet
PU.1-GFP
FcγR2/3low FLP
FcγR2/3+ FLP
EV
PU.1
Day 0
unstained
CellTrace Violet

Figure S6

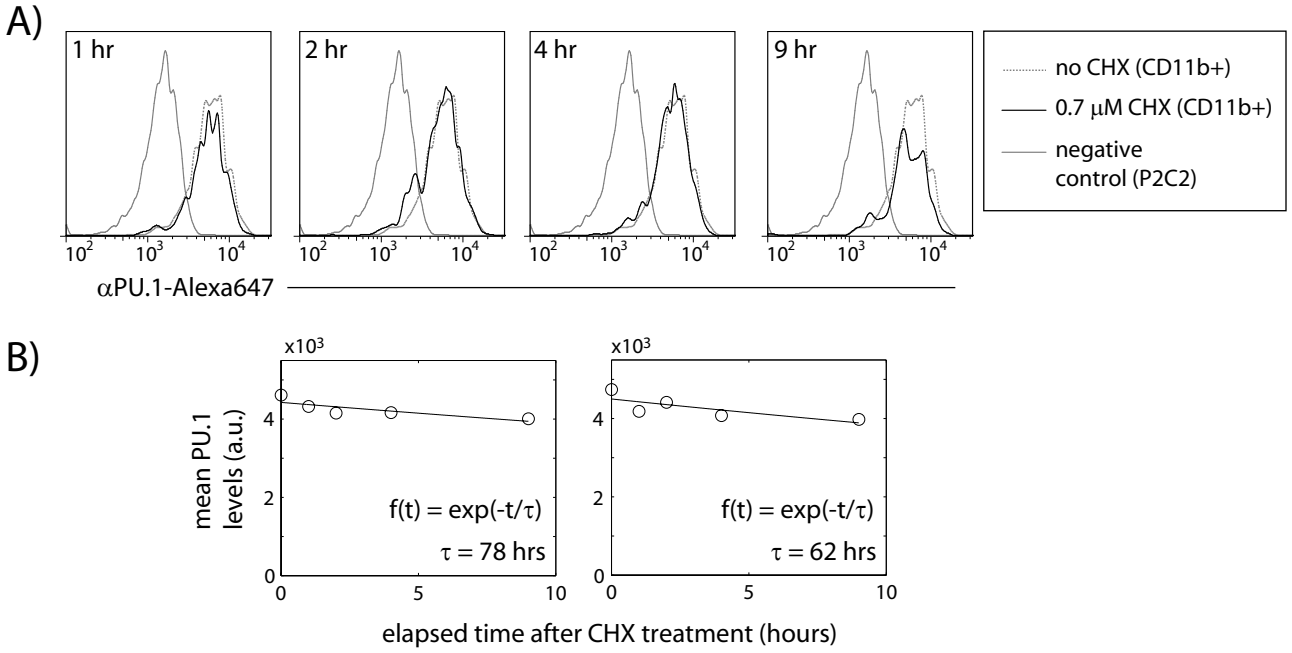
A)
1 hr
2 hr
4 hr
9 hr
no CHX (CD11b+)
0.7 μM CHX (CD11b+)
negative control (P2C2)
αPU.1-Alexa647
B)
x10³
mean PU.1 levels (a.u.)
f(t) = exp(-t/τ)
τ = 78 hrs
f(t) = exp(-t/τ)
τ = 62 hrs
elapsed time after CHX treatment (hours)

Figure S7

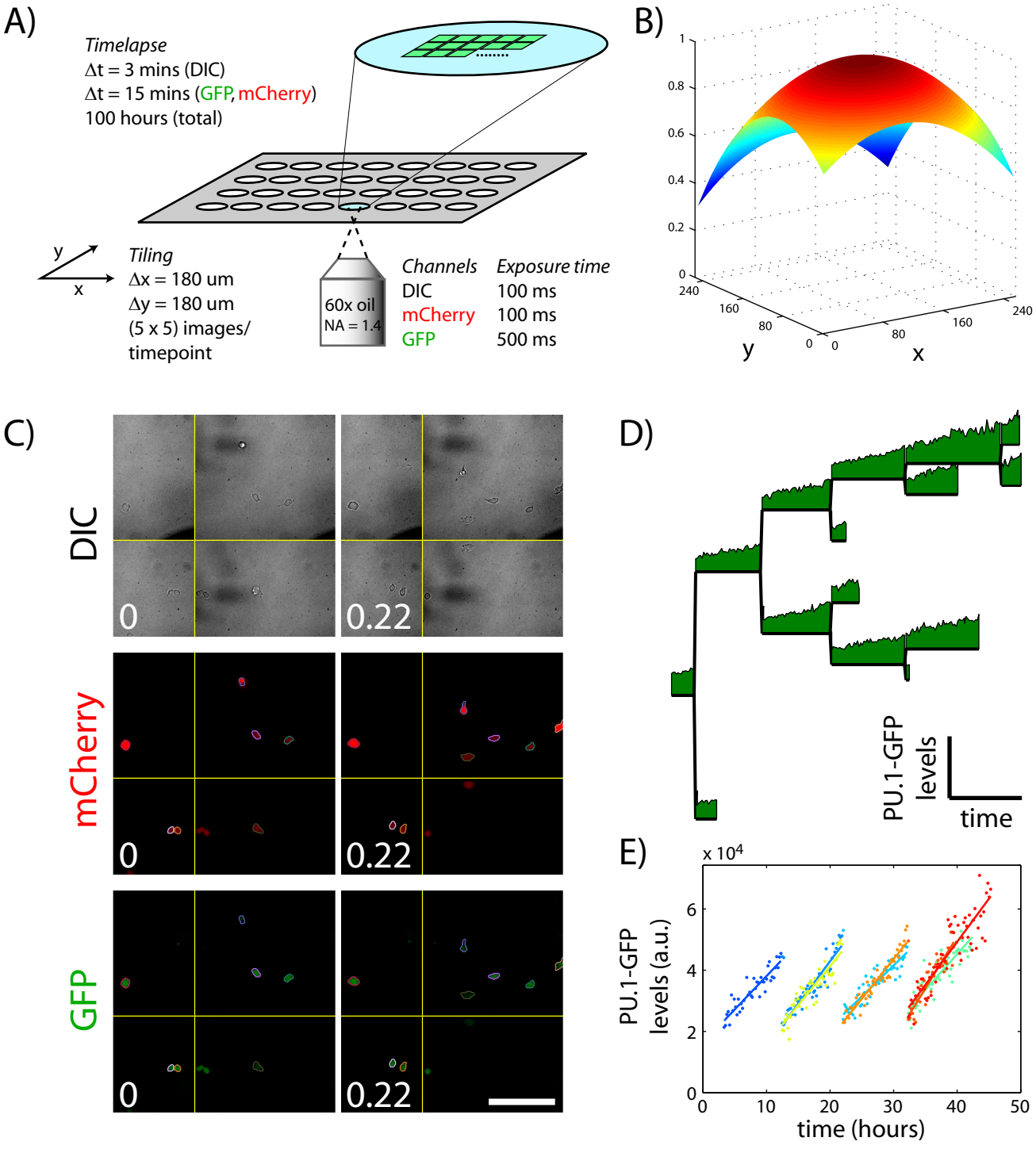
A)
Timelapse
Δt = 3 mins (DIC)
Δt = 15 mins (GFP, mCherry)
100 hours (total)
y
x
Tiling
Δx = 180 um
Δy = 180 um
(5 x 5) images/
timepoint
60x oil
NA = 1.4
Channels
DIC
mCherry
GFP
Exposure time
100 ms
100 ms
500 ms
B)
C)
DIC
mCherry
GFP
0
0.22
D)
PU.1-GFP
levels
time
E)
x 10^4
PU.1-GFP
levels (a.u.)
time (hours)

Figure S8

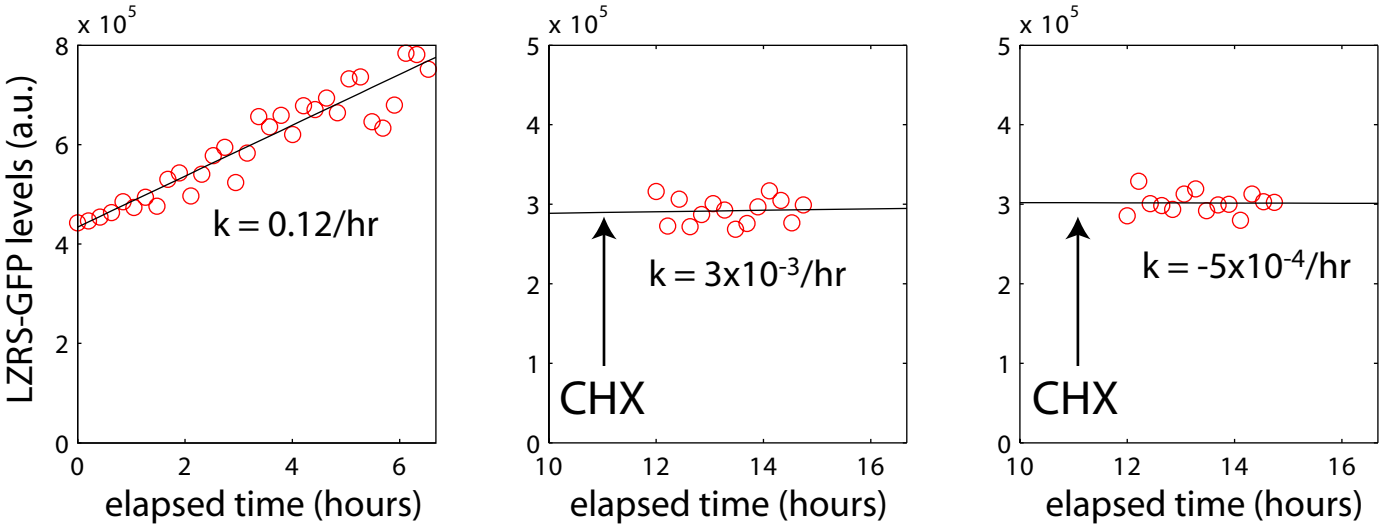
x 10^5
LZRS-GFP levels (a.u.)
k = 0.12/hr
elapsed time (hours)
x 10^5
k = 3x10^-3/hr
CHX
elapsed time (hours)
x 10^5
k = -5x10^-4/hr
CHX
elapsed time (hours)

Figure S9

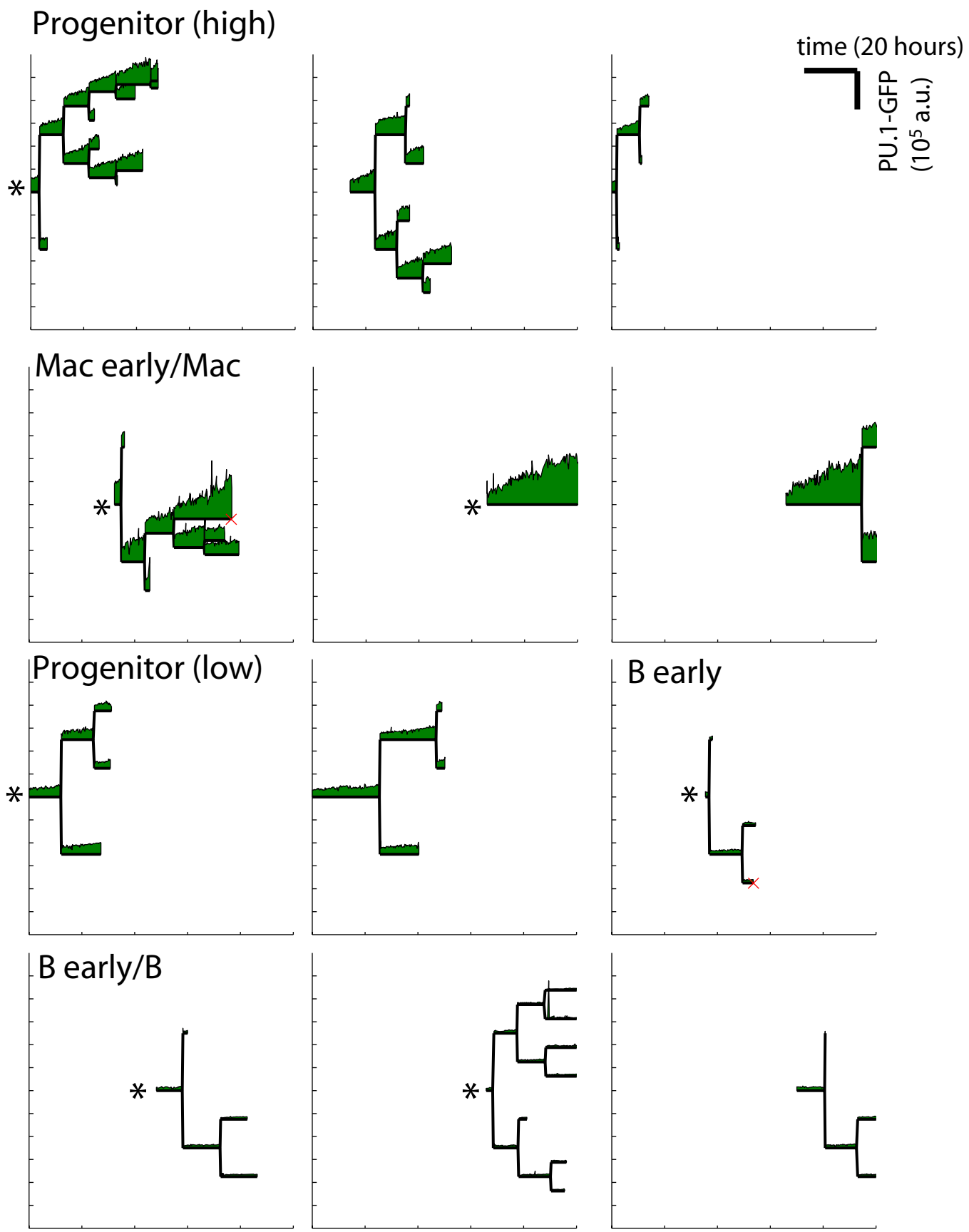
Progenitor (high)
time (20 hours)
PU.1-GFP
(10^5 a.u.)
Mac early/Mac
Progenitor (low)
B early
B early/B

Figure S10

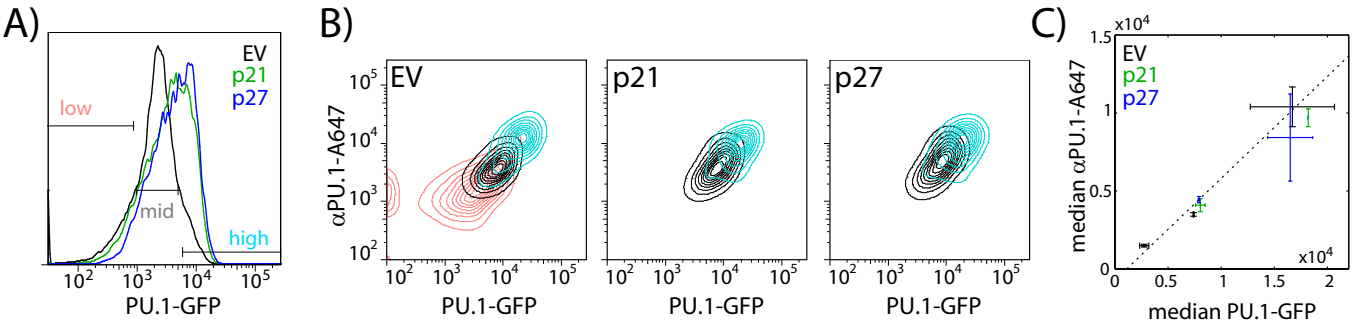
A)
EV
p21
p27
low
mid
high
PU.1-GFP
B)
EV
p21
p27
αPU.1-A647
PU.1-GFP
C)
x10^4
EV
p21
p27
median αPU.1-A647
median PU.1-GFP

Figure S11

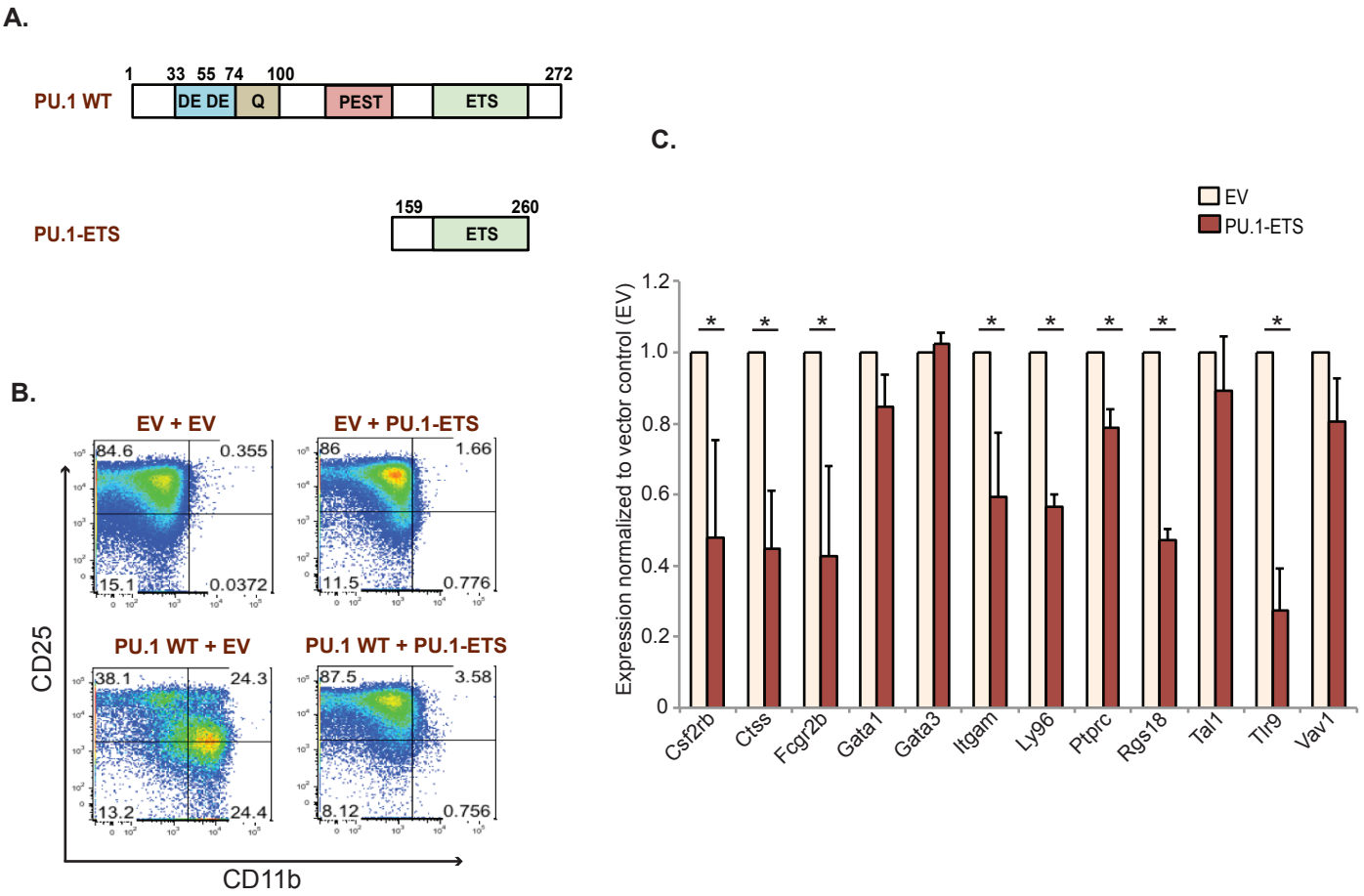
A.
PU.1 WT
1
33
55
74
100
272
DE DE
Q
PEST
ETS
PU.1-ETS
159
260
ETS
B.
EV + EV
EV + PU.1-ETS
PU.1 WT + EV
PU.1 WT + PU.1-ETS
84.6
0.355
15.1
0.0372
86
1.66
11.5
0.776
38.1
24.3
13.2
24.4
87.5
3.58
8.12
0.756
CD25
CD11b
C.
EV
PU.1-ETS
Expression normalized to vector control (EV)
1.2
1.0
0.8
0.6
0.4
0.2
0
Csf2rb
Ctss
Fcgr2b
Gata1
Gata3
Itgam
Ly96
Ptprc
Rgs18
Tal1
Tlr9
Vav1

Figure S12

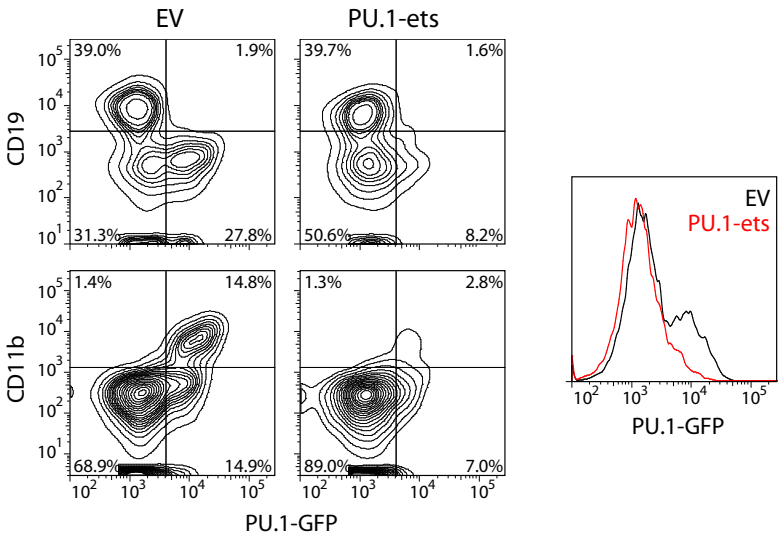
EV
PU.1-ets
CD19
CD11b
39.0%
1.9%
31.3%
27.8%
39.7%
1.6%
50.6%
8.2%
1.4%
14.8%
68.9%
14.9%
1.3%
2.8%
89.0%
7.0%
PU.1-GFP
EV
PU.1-ets
PU.1-GFP

Figure S13

EV-infected

PU.1 infected

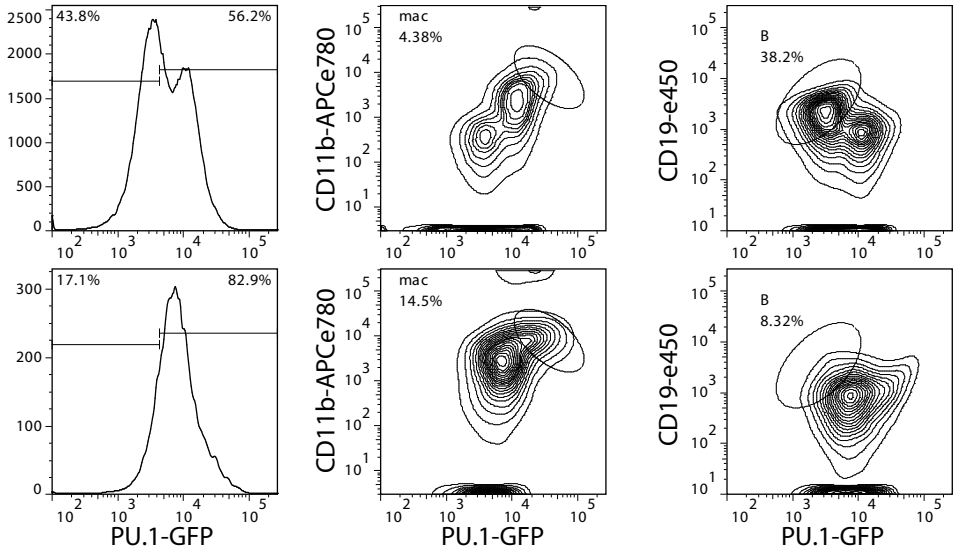

Figure S14

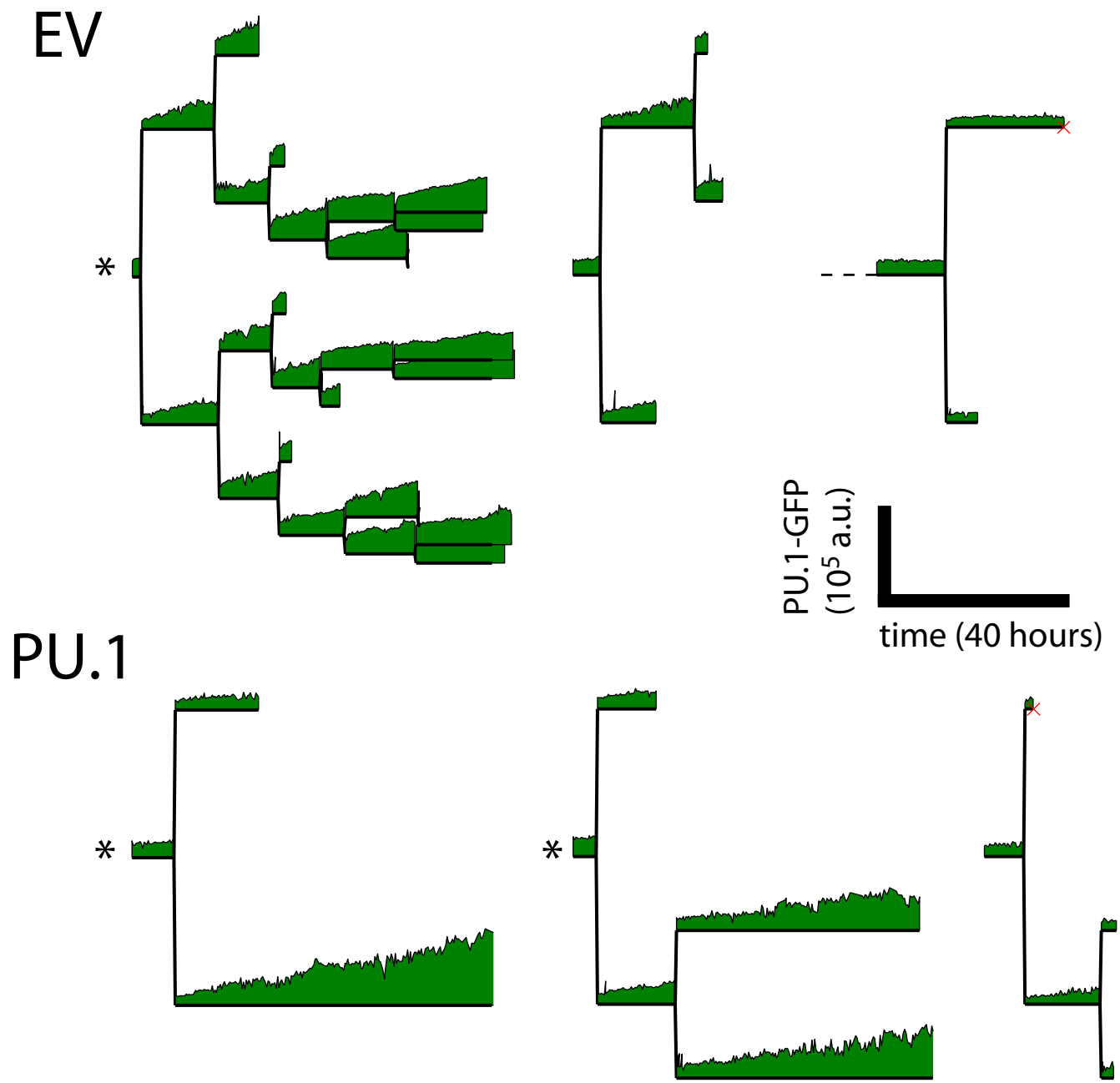

Figure S15

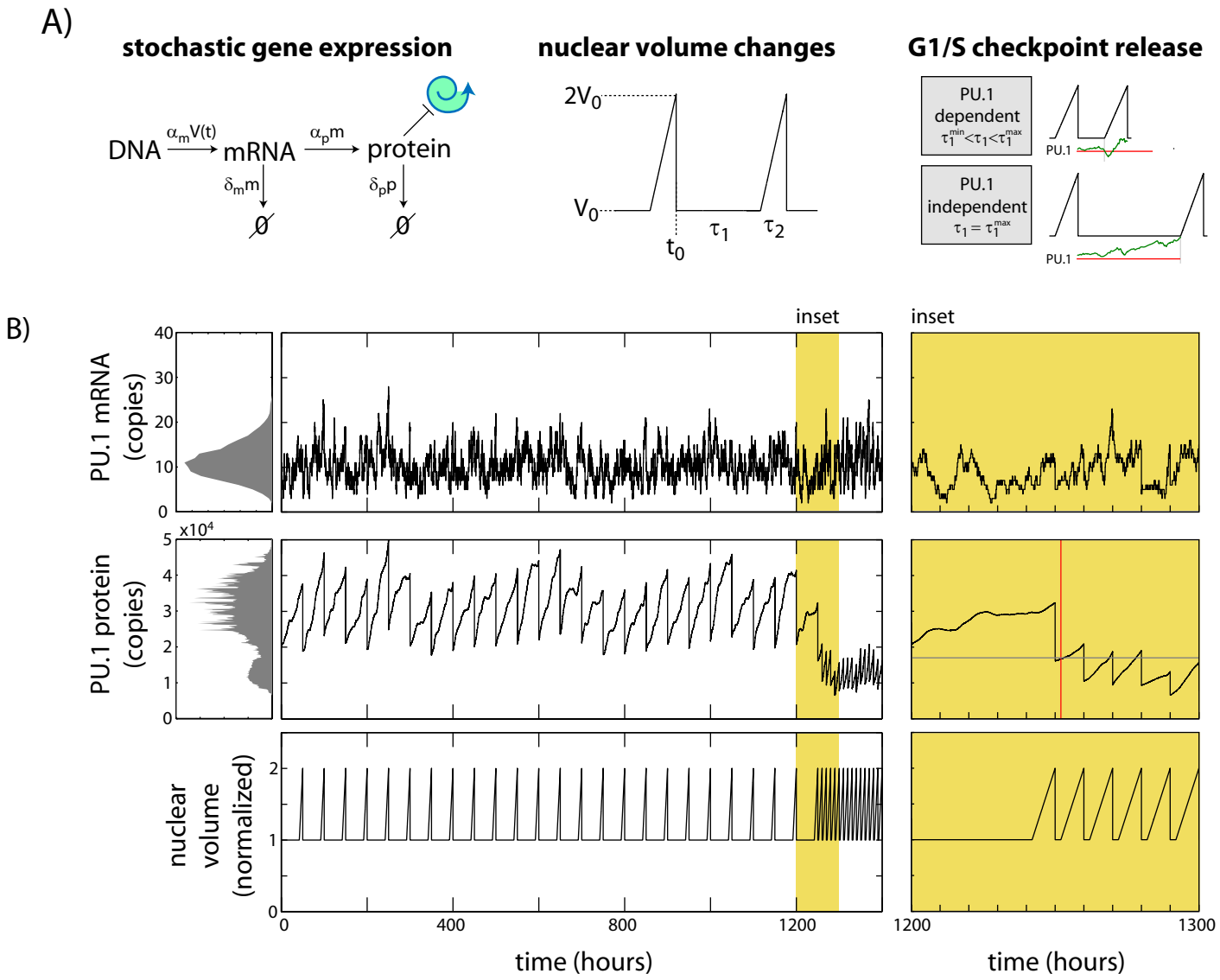
A)
stochastic gene expression
nuclear volume changes
G1/S checkpoint release
DNA
mRNA
protein
$\alpha_m V(t)$
$\alpha_p m$
$\delta_m m$
$\delta_p p$
$2V_0$
V_0
t_0
τ_1
τ_2
PU.1 dependent
$\tau_1^{min} < \tau_1 < \tau_1^{max}$
PU.1 independent
$\tau_1 = \tau_1^{max}$
PU.1
B)
inset
inset
PU.1 mRNA (copies)
PU.1 protein (copies)
x10^4
nuclear volume (normalized)
time (hours)
time (hours)

Figure S16

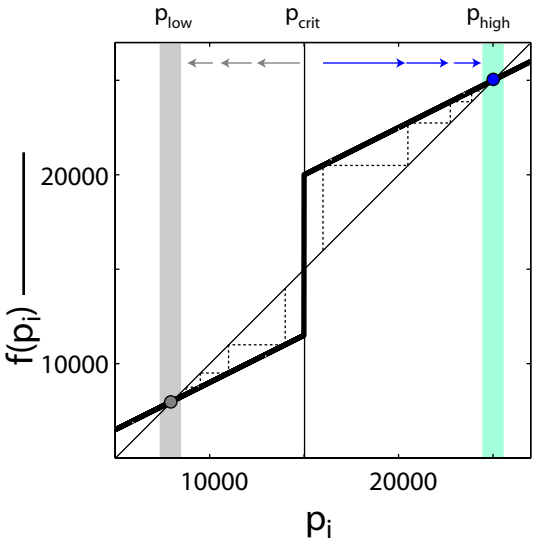

Figure S17

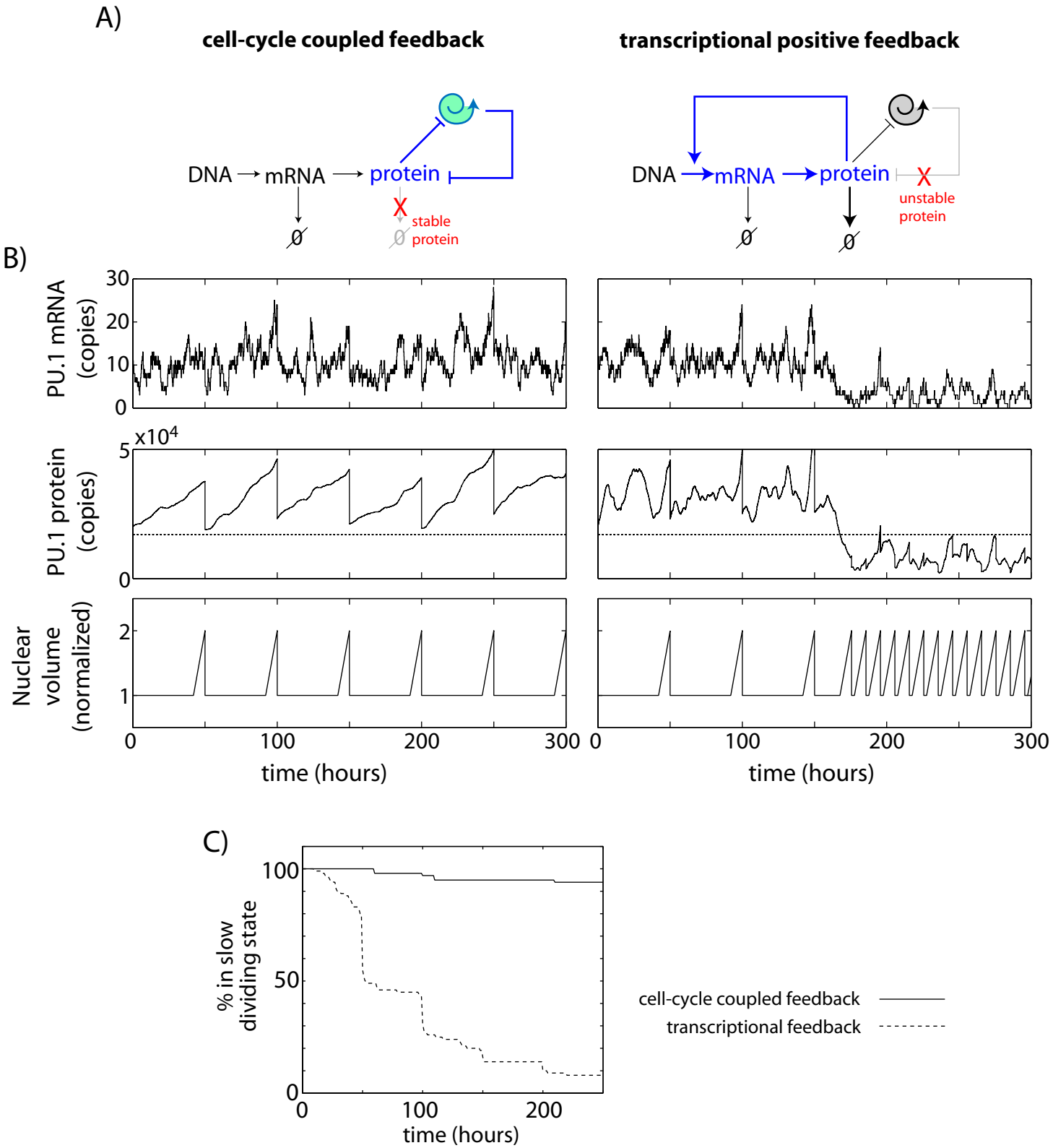
A)
cell-cycle coupled feedback
transcriptional positive feedback
DNA
mRNA
protein
stable protein
unstable protein
B)
PU.1 mRNA (copies)
PU.1 protein (copies)
x10^4
Nuclear volume (normalized)
time (hours)
C)
% in slow dividing state
time (hours)
cell-cycle coupled feedback
transcriptional feedback

Figure S18

Population A

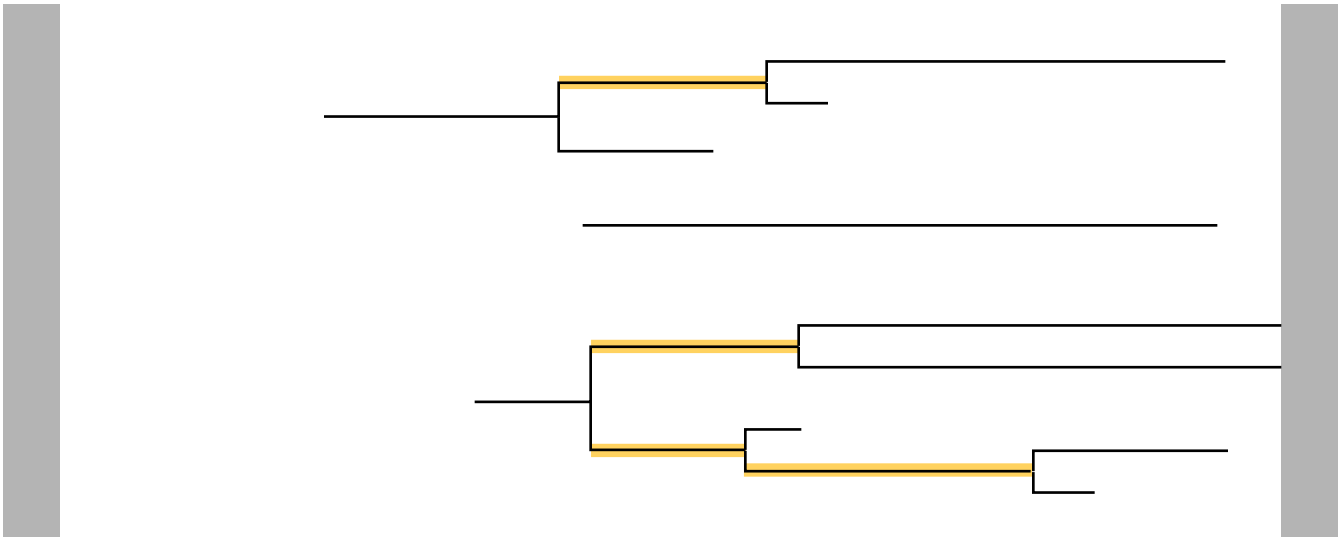

Population B

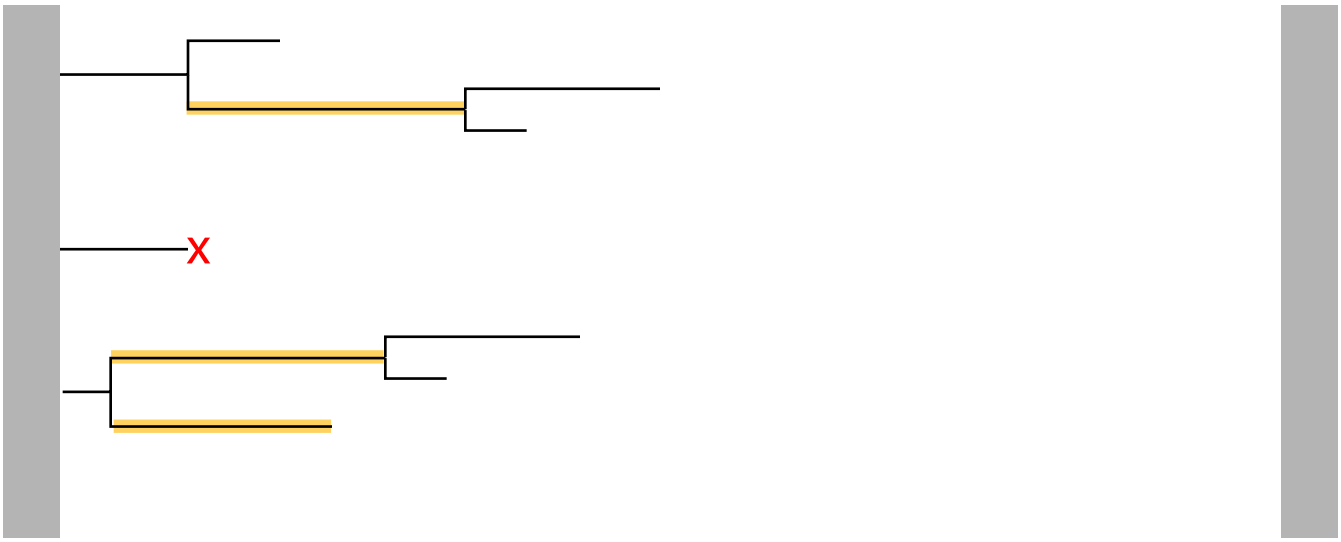

Table S1: List of antibodies

Antibody	**Clone**	**Supplier**	**Experimental Usage**
Ter119 biotin	TER-119	ebioscience	Depletion of lineage positive cells from fetal liver
F4/80 biotin	BM8	eBioscience	Depletion of lineage positive cells from fetal liver
Gr-1 biotin	RB6-8C5	eBioscience	Depletion of lineage positive cells from fetal liver
CD11c biotin	N418	eBioscience	Depletion of lineage positive cells from fetal liver
NK1.1 biotin	PK136	eBioscience	Depletion of lineage positive cells from fetal liver
CD19 biotin	eBio1D3	eBioscience	Depletion of lineage positive cells from fetal liver
cKit-APC-eFluor780	2B8	eBioscience	Sorting of fetal liver progenitors (Fig. 2, S2, S6, S5, S10, S12)
cKit-PacBlue	2B8	BioLegend	Sorting of fetal liver progenitors (Fig. 1, 3, S1, S3, S4, S10, S13, S14)
CD27-APC	PC61.5	eBioscience	Sorting of fetal liver progenitors (all experiments)
FcγR2/3 (CD16/32)- e450	93	eBioscience	Sorting of FcγR2/3 +/low fetal liver progenitors (Fig. 2C-D, 3E, S5, S6, S12)
Streptavidin-eFluor450		eBioscience	Sorting of fetal liver progenitors (Fig. S2)
Streptavidin-Brilliant Violet 570		Biolegend	Sorting of FcγR2/3 +/low fetal liver progenitors (Fig. 2C-D, 3E, S5, S6, S12)
Streptavidin-APC-eFluor780		eBioscience	Sorting of fetal liver progenitors (Fig. 1, 3, S1, S3, S4, S9, S13, S14)
Streptavidin-PerCP-Cy5.5		eBioscience	Sorting of fetal liver progenitors (Fig. S1, S10)
7-aminoactinmycin D		Invitrogen	Sorting of fetal liver progenitors (Fig. S1, S10)
CD19 PE	6D5	eBioscience	Flow cytometry analysis of cultured progenitors (Fig. 1, S2, S4)
Gr-1 APC	RB6-8C5	eBioscience	Flow cytometry analysis of cultured progenitors (Fig. 1, S4)
CD11b-APC-eFluor780	M1/70	eBioscience	Flow cytometry analysis of cultured progenitors (Fig. 1, 2, 3, S2, S4, S5, S12, S13)
CD11b-eFluor450	M1/70	eBioscience	Flow cytometry analysis of cultured progenitors (Fig. S6)
F4/80-eFluor450	BM8	eBioscience	Flow cytometry analysis of cultured progenitors (Fig. 1, S4)
CD19-eFluor450	eBio1D3	eBioscience	Flow cytometry analysis of cultured progenitors (Fig. S13)
CD19-PE	eBio1D3	eBioscience	Flow cytometry analysis of cultured progenitors (Fig. S12)
αPU.1-AlexaFluor647	9G7	Cell signaling and technology	Immunofluorescence staining of PU.1 protein in single cells (Fig. S3, S6)

Table S2: DNA constructs

Gene expressed	**Retroviral backbone**	**Experimental Usage**
IRES-mCherry (empty vector)	MSCV2.2	Segmentation of imaged cells (Fig. 1, 3, S7, S9, S14); Empty vector control (Fig. 2-3, S5, S12, S13, S14)
p21-IRES-mCherry	MSCV2.2	Induction of cell-cycle lengthening (Fig. 2B)
p27-IRES-mCherry	MSCV2.2	Induction of cell-cycle lengthening (Fig. 2B)
PU.1-IRES-mCherry	MSCV2.2	Test for PU.1 positive feedback regulation (Fig. 3, S5, S13)
PU.1-ets-IRES-mCherry	MSCV2.2	Test for role of high PU.1 in mediating myeloid differentiation by cell-cycle lengthening (Fig. 2C-D); Test for role of transcriptional positive feedback in PU.1 down-regulation (Fig. S12)
IRES-H2B-mCerulean (empty vector)	MSCV2.2	Empty vector control (Fig. S10). Color chosen to minimize interference with Alexa-647 αPU.1 antibody used for immunofluorescence staining
p21-IRES-H2B-mCerulean	MSCV2.2	Induction of cell-cycle lengthening, PU.1 immunofluorescence staining (Fig. S10)
p27-IRES- H2B-mCerulean	MSCV2.2	Induction of cell-cycle lengthening, PU.1 immunofluorescence staining (Fig. S10)
IRES-GFP (empty vector)	LZRS	Test of GFP imaging stability (Fig. S8) (*6*)

Table S3: Cytokines

Cytokine	**Concentration**	**Company**
Murine SCF	5 ng/mL	Peprotech
Murine IL-3	0.5 ng/mL (Fig. S2) 0.1 ng/mL (all others)	Peprotech
Human IL-7	5 ng/mL	Peprotech
Human Flt3L	5 ng/mL	Peprotech
Murine M-CSF	0.5 ng/mL (Fig. 1, S4), 5 ng/mL (Fig. S6)	Peprotech

Table S4: Primers for quantitative RT-PCR

Gene	Forward Primer	Reverse Primer
β-actin	ACA CCC GCC ACC AGT TC	TAC AGC CCG GGG AGC AT
PU.1 (exon3-4)	CTC AGT CAC CAG GTT TCC T	TCC AAG CCA TCA GCT TCT C
PU.1 (5' UTR)	GCA GGG GAT CTG ACC AA	CGT AAG TAA CCA AGT CAT CCG AT
Cyclin D2	GCA GGA TGA TGA AGT GAA CAC	GAG ACA ATC CAC ATC AGT GTG
Cdc25a	GAA TAA ATT CCC TAC CTC AGA AGC	TGT CGT GGT CTA GAG AAT CAG
Myb	GAA GAT GCT ACC TCA GAC C	ATT CCA GAT TCA TCC GAT TCC
Myc	CTG TAC CTC GTC CGA TTC C	GCT CTT CTT CAG AGT CGC T
p21	TTG CAC TCT GGT GTC TGA G	GTG ATA GAA ATC TGT CAG GCT G
Gfi1	AAT GCA GCA AGG TGT TCT C	CTT ACA GTC AAA GCT GCG T

symbol	description	parameter value		
		cell-cycle	transcriptional	hybrid
α_m	mRNA transcription rate	3 $hr^{-1}vol^{-1}$	N/A	N/A
$\alpha_m^{(1)}$	mRNA transcription rate (low)	N/A	1.25 $hr^{-1}vol^{-1}$	0.45 $hr^{-1}vol^{-1}$
$\alpha_m^{(2)}$	mRNA transcription rate (high)	N/A	3 $hr^{-1}vol^{-1}$	3 $hr^{-1}vol^{-1}$
δ_m	mRNA degradation rate	0.3 hr^{-1}	0.3 hr^{-1}	0.3 hr^{-1}
α_p	protein translation rate	100 hr^{-1}	922 hr^{-1}	100 hr^{-1}
δ_p	protein degradation rate	0.02 hr^{-1}	0.3 hr^{-1}	0.02 hr^{-1}
N	Hill coeff. for transcription activation	N/A	N/A	5
M	Hill coeff. for cell-cycle arrest	N/A	N/A	20
π_t	threshold for transcription activation	N/A	17000	5000
$\tau_1^{\min}$	minimum G1 duration	2 hr	2 hr	2 hr
$\tau_1^{\max}$	maximum G1 duration	42 hr	42 hr	42 hr
τ_2	S/G2/M duration (fixed)	42 hr	42 hr	42 hr
π_c	threshold for G1 arrest	17000	17000	17000
V_0	nuclear volume	1 vol	1 vol	1 vol

Table S5: Parameters values used for stochastic single-cell simulations of the cell-cycle coupled feedback loop (Fig. 4A, S15), transcriptional positive feedback loop (Fig. S17) and hybrid positive feedback loop (Fig. 4B). Rate constants for gene expression are loosely based on a recent global study of gene expression kinetics in mammalian cells [24]. Furthermore, parameters are chosen to recapitulate the following observations: 1) PU.1 has a protein half-life of ∼50 hours (Fig. S6), and this is incorporated into the cell-cycle couple feedback and hybrid feedback models (n.b. the hypothetical pure transcriptional feedback model has a considerably shorter PU.1 half-life, but this is necessary for the mathematically-controlled comparison of the two models, as we discuss in the text). 2) Macrophages have approximately three fold higher PU.1 levels compared to progenitors (Fig. 1); 3) Fast and slow-dividing cells have cell-cycle lengths of 10 and 50 hours respectively (Fig. 1); 4) For the hybrid feedback loop model, Hill coefficients match the experimentally observed number of discrete sites of PU.1 occupancy on its own cis-regulatory elements [11]. 5) Additionally, gene expression kinetic parameters are chosen such that the steady-state number of copies of PU.1 protein is comparable to the number of PU.1 binding sites in the genome ($\sim 10^4$/cell), as measured by deep-sequencing [43].

symbol	**description**	**parameter value**	
		cell-cycle	hybrid
A_0	protein synthesis rate (no feedback)	1500 hr^{-1}	N/A
A_{min}	basal protein synthesis rate	N/A	165 hr^{-1}
A_{max}	maximal protein synthesis rate	N/A	1500 hr^{-1}
C_{max}	maximum cell division rate	0.1 hr^{-1}	0.1 hr^{-1}
C_{min}	minimum cell division rate	0.02 hr^{-1}	0.02 hr^{-1}
K_p	PU.1 level for half-maximal transcriptional activation	N/A	6000
K_c	PU.1 level for half-maximal cell-cycle arrest	20000	20000
M	Hill coefficient for transcriptional activation	N/A	5
N	Hill coefficient for cell-cycle arrest	20	20
D	protein degradation rate	0.02 hr^{-1}	0.02 hr^{-1}

Table S6: Parameters values used for phase plane analysis of the cell-cycle coupled feedback loop and the hybrid feedback loop (Fig. 4C). Parameters are chosen to loosely correspond to those analyzed in the stochastic single-cell models (Table S5).